Peer-reviewed version available at Entropy 2018, 20, 680; doi:10.3390/e20090680

Article

Evaporation Boundary Conditions for the Linear R13 Equations based on the Onsager Theory

Alexander Felix Beckmann [1,*], Anirudh Singh Rana [2], Manuel Torrilhon [3] and Henning Struchtrup [1]

[1] Department of Mechanical Engineering, University of Victoria, Victoria, British Columbia V8W 3P6, Canada; struchtr@uvic.ca (H.S.)
[2] Mathematics Institute, University of Warwick, Warwick, United Kingdom; anirudh@uvic.ca
[3] Center for Computational Engineering Science (CCES), RWTH Aachen University, Aachen, Germany; mt@mathcces.rwth-aachen.de
* Correspondence: beckmann@uvic.ca; Tel.: +1-778-922-4221

Abstract: Due to failure of the continuum hypothesis for higher Knudsen numbers, rarefied gases and microflows of gases are particularly difficult to model. Macroscopic transport equations compete with particle methods, such as DSMC to find accurate solutions in the rarefied gas regime. Due to growing interest in micro flow applications, such as micro fuel cells, it is important to model and understand evaporation in this flow regime. Here, evaporation boundary conditions for the R13 equations, which are macroscopic transport equations with applicability in the rarefied gas regime, are derived. The new equations utilize Onsager relations, linear relations between thermodynamic fluxes and forces, with constant coefficients, that need to be determined. For this, the boundary conditions are fitted to DSMC data and compared to other R13 boundary conditions from kinetic theory and Navier-Stokes-Fourier (NSF) solutions for two one-dimensional steady-state problems. Overall, the suggested fittings of the new phenomenological boundary conditions show better agreement to DSMC than the alternative kinetic theory evaporation boundary conditions for R13. Furthermore, the new evaporation boundary conditions for R13 are implemented in a code for the numerical solution of complex, two-dimensional geometries and compared to NSF solutions. Different flow patterns between R13 and NSF for higher Knudsen numbers are observed.

Keywords: rarefied gas dynamics; modelling evaporation; R13-equations

1. Introduction

For modeling ideal gas flow, there are in general two approaches, the microscopic and the macroscopic approach. In the microscopic approach the Boltzmann equation [1][2] is solved, e.g., with the Direct Simulation Monte Carlo method (DSMC) [3]. However, tracking particles is computationally expensive and for engineering applications determining the macroscopic quantities is often sufficient. In the macroscopic approach, microscopic information is condensed into quantities such as mass density, bulk velocity, temperature, heat flux and stress. Macroscopic transport equations reduce the number of variables and when simplified allow for analytical solutions. The advantage of faster calculations is associated with the restriction to certain flow regimes. Flow regimes can be characterized by the Knudsen number, which is the ratio of the mean free path, i.e., the average distance a molecule travels between two subsequent collisions, and a characteristic length, e.g., the diameter of a pipe. For Knudsen numbers larger than $\mathrm{Kn} \approx 4 \cdot 10^{-2}$ [4] the classical Navier-Stokes-Fourier (NSF) equations start to fail [4][5]. Applications for Knudsen numbers in the transition regime, i.e., $4 \cdot 10^{-2} < \mathrm{Kn} < 2.5$ [4] may be those with large mean free paths, e.g., in vacuum or aerospace applications, or those with small characteristic lengths, which can be found in microflows. In this regime rarefaction effects are observed, such as temperature jump and velocity slip at interfaces, Knudsen layers in front of interfaces, transpiration flow, thermal stresses, or heat transfer without temperature gradients

[4][5][6][7][8]. Knudsen layers are thin areas in front of boundaries in the order of a few mean free paths, where particle interaction with the boundary is the dominant mechanism.

By combining the Grad and Chapmann-Enskog methods into the new order of magnitude method, Struchtrup and Torrilhon proposed the regularized R13 equations, macroscopic transport equations which account for effects in the transition regime [9]. Like all macroscopic transport equations, the R13 equations are an approximation of the Boltzmann equation. R13 introduces higher moments which have a large influence in the rarefied gas regime and small influence in the regime of small Knudsen numbers. Coefficients within the R13 equations allow quick adjustment between different collision models, such as Maxwell molecules, hard-spheres (HS) or the Bhatnager-Gross-Krook (BGK) model [5]. In the following, only Maxwell molecules will be considered.

Due to increasing interest in microelectromechanical devices (MEMS) [10], it is of interest to model evaporation processes for Knudsen numbers in the transition regime.

Based on microscopic boundary conditions of the Boltzmann equation, Struchtrup et al. derived macroscopic boundary conditions for R13 [11]. These equations, which are referred to as MBC (Macroscopic Boundary Conditions) in the following, show promising results for Knudsen numbers in the transition regime. Here we seek to derive improved evaporation boundary conditions by using an entropy balance integrated around an interface between liquid and vapor phase. Based on the Onsager theory, the integrated entropy balance is rewritten as sum of thermodynamic fluxes and forces [12]. The Onsager theory assumes linear relations between fluxes and forces and allows to break the entropy balance into sets of equations, which we utilize as evaporation/condensation boundary condtions [13][14].

A challenge lies in determining the Onsager coefficients, which provide the linear relations between fluxes and forces. The linear R13 equations, accompanied by the new phenomenological boundary conditions (PBC), are solved for two one-dimensional, steady-state configurations. The first system consists of a vapor phase between two liquid reservoirs. A DSMC solution for this set-up is used to fit the Onsager coefficients and to compare the results with the macroscopic boundary conditions for R13 and also with two Navier-Stokes-Fourier models, which are based on the Onsager theory as well. The second configuration is a half space problem [15], for which dimensionless flow parameters are used to compare the different models.

The remainder of the paper proceeds as follows: Section 1 gives an overview of the R13 equations and the corresponding macroscopic evaporation boundary conditions, based on kinetic theory. Section 2 explains the derivation of the Onsager boundary conditions. Section 3 shows how the Onsager coefficients are determined, mainly by fitting to DSMC data. In Sec. 4 the newly derived boundary conditions are put to test in a numerical steady-state simulation with complex geometries. The work is summarized and discussed in Sec. 5.

1.1. The R13 Equations

In the following all equations are non-dimensionalized and linearized around an equilibrium state defined by a reference density for the vapor ρ_0 and reference temperature T_0. The equilibrium saturation pressure for both liquid and vapor is defined as $p_0 = p_{sat}(T_0)$. We shall consider small deviations from equilibrium, caused by pressure or temperature gradients, to drive evaporation or condensation. Non-dimensionalizing allows to introduce meaningful coefficients into the equations, e.g., Prandtl or Knudsen numbers. The connection between variables denoting non-dimensional deviation to an equilibrium state (with hat) and the regular variables with dimension is

$$T = T_0\left(1+\widehat{T}\right)\,,\quad \rho = \rho_0\left(1+\widehat{\rho}\right)\,,\quad p = p_0\left(1+\widehat{p}\right)\,, \tag{1}$$

$$v_k = \sqrt{RT_0}\widehat{v}_k\,,\quad q_k = \rho_0\sqrt{RT_o}^3\widehat{q}_k\,,\quad \sigma_{ik} = \rho_0 RT_0\widehat{\sigma}_{ik}\,,$$

$$h = h_0\left(1+\widehat{h}\right)\,,\quad u = u_0\left(1+\widehat{u}\right)\,,\quad \eta = \rho s = \eta_0\left(1+\widehat{\eta}\right)\,,$$

$$x_k = L\widehat{x}_k\,, \quad t = \frac{L}{\sqrt{RT_0}}\widehat{t}\,.$$

Here, T is temperature, ρ mass density, p pressure, v_k velocity vector, q_k heat flux vector, σ_{ik} stress tensor, h enthalpy, u internal energy, $\eta = \rho s$ entropy density, x_k position vector and t time. From now on, the hats are not shown.

The governing macroscopic equations that describe the gas are given by the conservation laws for mass, momentum and energy, which in linearized and dimensionless form, read

$$\frac{\partial \rho}{\partial t} + \frac{\partial v_k}{\partial x_k} = 0\,, \tag{2}$$

$$\frac{\partial v_i}{\partial t} + \frac{\partial \sigma_{ik}}{\partial x_k} + \frac{\partial p}{\partial x_i} = F_i\,, \tag{3}$$

$$\frac{3}{2}\frac{\partial T}{\partial t} + \frac{\partial v_k}{\partial x_k} + \frac{\partial q_k}{\partial x_k} = 0\,. \tag{4}$$

Here, F_i is a body force, e.g., gravitational force. One has five equations for the five unknowns ρ, v_i and T. An algebraic equation for p is found in the ideal gas law $p = \rho RT$, which assumes for the non-dimensional and linear case the form $p = \rho + T$, with all variables describing the deviation to the equilibrium state.

It is necessary to find equations for the heat flux vector q_k and stress tensor σ_{ik}, which beyond the hydrodynamic regime become full balance equations. By means of the order of magnitude method, Struchtrup & Torrilhon derived the following (here linearized & non-dimensionalized) balance equations from the Boltzmann equation, known as the regularized 13 moment equations, Ref. [9],

$$\frac{\partial \sigma_{ij}}{\partial t} + \frac{4}{5}\,\mathrm{Pr}\,\frac{\overline{w}_3}{\overline{w}_2}\frac{\partial q_{\langle i}}{\partial x_{j\rangle}} + \frac{\partial m_{ijk}}{\partial x_k} = -\frac{2}{\overline{w}_2}\frac{1}{\mathrm{Kn}}\left[\sigma_{ij} + 2\mathrm{Kn}\frac{\partial v_{\langle i}}{\partial x_{j\rangle}}\right]\,, \tag{5}$$

$$\frac{\partial q_i}{\partial t} + \frac{5}{4\,\mathrm{Pr}}\frac{\theta_4}{\theta_2}\frac{\partial \sigma_{ik}}{\partial x_k} + \frac{1}{2}\frac{\partial R_{ik}}{\partial x_k} + \frac{1}{6}\frac{\partial \Delta}{\partial x_i} = -\frac{1}{\theta_2}\frac{5}{2\,\mathrm{Pr}}\frac{1}{\mathrm{Kn}}\left[q_i + \frac{5}{2\,\mathrm{Pr}}\mathrm{Kn}\frac{\partial T}{\partial x_i}\right]\,. \tag{6}$$

The higher moments are defined over the relations

$$\Delta = -\frac{8\mathrm{Kn}}{\mathrm{Pr}_\Delta}\frac{\partial q_k}{\partial x_k}\,, \tag{7}$$

$$R_{ij} = -\frac{28}{5}\frac{\mathrm{Kn}}{\mathrm{Pr}_R}\frac{\partial q_{\langle i}}{\partial x_{j\rangle}}\,, \tag{8}$$

$$m_{ijk} = -\frac{3\mathrm{Kn}}{\mathrm{Pr}_M}\frac{\partial \sigma_{\langle ij}}{\partial x_{x\rangle}}\,. \tag{9}$$

By using the Chapman-Enskog expansion, while considering low Knudsen numbers, Eqs. (5,6) reduce to the laws of Navier-Stokes and Fourier, i.e., the left hand sides become zero [5]. The balance laws (5,6) use the higher moments Δ, R_{ik} and m_{ijk}. Here, $\mathrm{Pr} = \frac{\mu c_p}{k}$ denotes the Prandtl number, with μ as the shear viscosity. For a monatomic gas one has $c_p = \frac{5}{2}R$ as the isobaric specific heat and $k = \frac{15}{4}\mu$ as the thermal conductivity. The Knudsen number is $\mathrm{Kn} = \frac{\mu\sqrt{RT}}{pL}$, with L as characteristic length, e.g., the diameter of a pipe. Here, θ_2, θ_4, $\overline{w}_2$ and $\overline{w}_3$ are coefficients for different collision models, such as Maxwell, HS and BGK models. In the following sections only Maxwell molecules are considered, nevertheless the corresponding coefficients for Maxwell, Hard Sphere or BGK models for stress tensor, heat flux vector and higher moments can be found in Table 1 [12].

Table 1. Coefficients for Maxwell (MM), Hard Sphere (HS) and Bhatnager-Gross-Krook (BGK) models for the R13 equations.

	ϖ_2	$\varpi_3 = \theta_4$	θ_2	Pr	Pr_R	Pr_M	Pr_Δ
MM	2	3	45/8	2/3	7/6	3/2	2/3
BGK	2	2	5/2	1	1	1	1
HS	2.02774	2.42113	5.81945	0.6609	1.3307	1.3951	0.9025

1.2. Macroscopic Evaporation Boundary Conditions for Maxwell Molecules

For the case that a vapor molecule hitting the liquid interface is reflected back to the vapor and not being absorbed, Maxwell proposed an accommodation model, which is based on the assumption that the fraction χ of the vapor molecules hitting the liquid surface are diffusively reflected, i.e., with momentum and energy exchange, and the remaining fraction $(1-\chi)$ is specularly reflected, without energy exchange [7].

Based on microscopic evaporation boundary conditions of the Boltzmann equation, which are derived from a Maxwell model for the interface, Struchtrup et al. derived macroscopic evaporation boundary conditions (MBC) for the R13 equations [11]. In these, interface effects are described through the accommodation coefficient χ and the evaporation coefficient ϑ. The evaporation coefficient equals the condensation coefficient, which is the probability that a vapor particle hitting the liquid interface will condense [16].

After non-dimensionalization and linearization around an equilibrium state, the MBC for evaporation [11] read

$$V_n = \sqrt{\frac{2}{\pi}}\frac{\vartheta}{2-\vartheta}\left(p_{sat}\left(T^l\right) - p^g + \frac{1}{2}\left(T^g - T^l\right) - \frac{1}{2}\sigma^g_{nn} + \frac{1}{120}\Delta + \frac{1}{28}R_{nn}\right), \tag{10}$$

$$q^g_n = -\sqrt{\frac{2}{\pi}}\frac{\vartheta+\chi(1-\vartheta)}{2-\vartheta-\chi(1-\vartheta)}\left(2\left(T^g - T^l\right) + \frac{1}{2}\sigma^g_{nn} + \frac{1}{15}\Delta + \frac{5}{28}R_{nn}\right) - \frac{1}{2}V^g_n, \tag{11}$$

$$m_{nnn} = \sqrt{\frac{2}{\pi}}\frac{\vartheta+\chi(1-\vartheta)}{2-\vartheta-\chi(1-\vartheta)}\left(\frac{2}{5}\left(T^g - T^l\right) - \frac{7}{5}\sigma^g_{nn} + \frac{1}{75}\Delta - \frac{1}{14}R_{nn}\right) - \frac{2}{5}V^g_n, \tag{12}$$

$$\overline{\sigma}_{nk} = -\sqrt{\frac{2}{\pi}}\frac{\vartheta+\chi(1-\vartheta)}{2-\vartheta-\chi(1-\vartheta)}\left(\overline{V}^g_k + \frac{1}{5}\overline{q}^g_k + \frac{1}{2}\overline{m}_{nnk}\right), \tag{13}$$

$$\overline{R}_{nk} = \sqrt{\frac{2}{\pi}}\frac{\vartheta+\chi(1-\vartheta)}{2-\vartheta-\chi(1-\vartheta)}\left(\overline{V}^g_k - \frac{11}{5}\overline{q}^g_k - \frac{1}{2}\overline{m}_{nnk}\right), \tag{14}$$

$$\widetilde{m}_{nij} = -\sqrt{\frac{2}{\pi}}\frac{\vartheta+\chi(1-\vartheta)}{2-\vartheta-\chi(1-\vartheta)} \left(\widetilde{\sigma}^g_{ij} + \frac{1}{14}\widetilde{R}_{ij} + \left(\frac{1}{5}\left(T^g - T^l\right) - \frac{1}{5}\sigma^g_{nn} + \frac{1}{150}\Delta\right)\delta_{ij}\right) + \frac{1}{5}\delta_{ij}V^g_n. \tag{15}$$

Here, the index n refers to the direction normal to the interface. The Einstein notation, i.e., $A_{jj} = \sum_{j=1}^{3} A_{jj}$ is not applicable for the index n. The variables are tensor components, where the overbar denotes the normal-tangential- and tilde the tangential-tangential parts, see Appendix A. Note, that all variables describe the deviation to an equilibrium state.

2. Evaporation Boundary Conditions for linear R13 based on the 2nd Law of Thermodynamics

The MBC have the major drawback of stability problems, see [17]. Therefore, we aim to derive stable phenomenological boundary conditions (PBC) for the regularized R13 equations for a liquid-gas

interface. The approach follows Ref. [12], in which a reduced entropy balance is used to derive boundary conditions for a wall-gas interface. The entropy balance for a fluid with dimensionless entropy density $\widetilde{\eta}$, entropy flux Ψ_k and entropy generation rate Σ_{gen} reads

$$\frac{\partial \widetilde{\eta}}{\partial t} + \frac{\partial \Psi_k}{\partial x_k} = \Sigma_{gen} \, . \tag{16}$$

Eq. (16) shall be integrated over a small volume of area ΔA and height Δz across the liquid-vapor interface. By using Gauss' Theorem the integrated entropy balance becomes

$$\int\limits_{\Delta A \Delta z} \frac{\partial \widetilde{\eta}}{\partial t} dV + \oint\limits_{\partial \Delta V} \Psi_k n_k dA = \int\limits_{\Delta A \Delta z} \Sigma_{gen} dV \, . \tag{17}$$

For $\Delta z \to 0$ the first term vanishes and (17) reduces to the entropy balance for the interface,

$$\left(\Psi_k^g - \Psi_k^l \right) n_k = \Sigma_{surface} \geq 0 \, . \tag{18}$$

Hence, the entropy generation rate $\Sigma_{surface} = \frac{1}{dA} \int\limits_{\Delta A \Delta z} \Sigma_{gen} dV$ is equal to the difference in entropy fluxes entering and leaving the interface. In the following, all variables on liquid side are denoted with l and all variables on vapor side with g. A linear combination of manipulated mass, energy and entropy balances (Appendix B) leads to the (linearized and non-dimensional) entropy flux on liquid side as

$$\Psi_k^l = -q_k^l T^l - \sigma_{ik}^l v_i^l - p^l v_k^l \, . \tag{19}$$

Here T, ρ and v are deviations from an equilibrium state defined by T_0, ρ_0 and $p_0 = p_{sat}\left(T_0\right)$. For the linear R13 equations and the vapor side, the linearized and dimensionless entropy flux (Appendix B) is

$$\Psi_k^g = -\left(\rho^g + T^g\right) v_k^g - v_i^g \sigma_{ik}^g - T^g q_k^g - \frac{\omega_3}{5} \, \mathrm{Pr} \, q_i^g \sigma_{ik}^g - \frac{\omega_2}{4} \sigma_{ij}^g m_{ijk} - \frac{2\theta_2}{25} \left(\mathrm{Pr}\right)^2 \left(q_i^g R_{ik} + \frac{\Delta}{3} q_k^g \right) \, . \tag{20}$$

Furthermore, the (linearized and non-dimensional) balance laws for mass, momentum and energy, integrated around the interface similar to (18) become

$$\rho_l v_k^l n_k = \rho_0 v_k^g n_k \, , \tag{21}$$

$$p^l n_i + \sigma_{ik}^l n_k = p^g n_i + \sigma_{ik}^g n_k \, , \tag{22}$$

$$\frac{\rho_l h_0^l}{R \rho_0 T_0} v_k^l n_k + q_k^l n_k = \frac{h_o^g}{R T_o} v_k^g n_k + q_k^g n_k \, . \tag{23}$$

The variables v_k^l and v_k^g are the velocities on the liquid and vapor sides from the perspective of an observer resting on the interface.

The entropy fluxes (19,20) are plugged into the integrated entropy balance (18). Eqs. (21-23) are used to eliminate the variables v_k^l, σ_{ik}^l and q_k^l. All variables describe the deviation to equilibrium, are dimensionless and linearized. After applying the appropriate coefficients for Maxwell molecules, according to Table 1, using the Clausius Clapeyron equation [18] (linearized and dimensionless) in the form $p_{sat}\left(T^l\right) = \frac{h_{gl}^0}{R T_0} T^l$ and by considering $\rho_l \gg \rho_0$, one may write (18) as

$$J_k^g n_k \frac{1}{\rho_0} \left(p_{sat}\left(T^l\right) - p^g \right) - \left(T^g - T^l \right) q_k^g n_k - V_i \sigma_{ik}^g n_k - \frac{\omega_3}{5} \, \mathrm{Pr} \, q_i^g \sigma_{ik}^g n_k$$
$$- \frac{\omega_2}{4} \sigma_{ij}^g m_{ijk} n_k - \frac{2\theta_2}{25} \left(\mathrm{Pr}\right)^2 \left(q_i^g R_{ik} n_k + \frac{\Delta}{3} q_k^g n_k \right) = \Sigma_{surface} \geq 0 \, , \tag{24}$$

where $V_i = v_i^g - v_i^l$, $J_k^g n_k = \rho_0 v_k^g n_k$ and the corresponding ideal gas law, given as $\rho^g = p^g - T^g$ was used. To accomplish a proper entropy balance for the linearized equations, terms up to second order are kept [19].

Next, the entropy balance is split into contributions from normal and tangential components, see Appendix A; all matrices and higher moments are symmetric and trace free,

$$\begin{aligned}\Sigma_{surface} = J_n^g \frac{1}{\rho_0}\left[p_{sat}\left(T^l\right) - p^g - \sigma_{nn}\right] \\ + q_n^g\left[-\left(T^g - T^l\right) - \frac{\omega_3}{5}\,\mathrm{Pr}\,\sigma_{nn} - \frac{2\theta_2}{25}\,(\mathrm{Pr})^2\left(R_{nn} + \frac{\Delta}{3}\right)\right] \\ + m_{nnn}\left[-\frac{3\omega_2}{8}\sigma_{nn}\right] \\ + \overline{\sigma}_{nk}\left[-\overline{V}_k - \frac{\omega_3}{5}\,\mathrm{Pr}\,\overline{q}_k - \frac{\omega_2}{2}\overline{m}_{nnk}\right] + \overline{R}_{nk}\left[-\frac{2\theta_2}{25}\,(\mathrm{Pr})^2\,\overline{q}_k\right] \\ + \widetilde{m}_{nij}\left[-\frac{\omega_2}{4}\widetilde{\sigma}_{ij}\right] \qquad .\end{aligned} \tag{25}$$

As before, overbar denotes normal-tangential and tilde denotes tangential-tangential components. In case that the mass flow J_n^g vanishes, Eq. (25) simplifys to the entropy generation at a wall-gas-interface, see Ref. [12].

The entropy generation may be written as a superposition of thermodynamic fluxes J_i and forces X_i, [13][14]:

$$\Sigma_{surface} = \sum_i J_i X_i \geq 0\,. \tag{26}$$

Here, moments with odd degree in the normal direction n are identified as fluxes, i.e., J_n, q_n, m_{nnn}, $\overline{\sigma}_{nk}$, $\overline{R}_{nk}$ and $\widetilde{m}_{nij}$, while moments with even degree in n are identified as the corresponding forces, i.e., p^g, T^g, T^l, σ_{nn}, R_{nn}, Δ, $\overline{V}_k$, $\overline{q}_k$, $\overline{m}_{nnk}$ and $\widetilde{\sigma}_{ij}$. Note that p^g, T^g, T^l, σ_{nn}, R_{nn}, Δ, J_n, q_n and m_{nnn} are scalars, $\overline{V}_k$, $\overline{q}_k$, $\overline{m}_{nnk}$, $\overline{\sigma}_{nk}$ and $\overline{R}_{nk}$ are vectors, and $\widetilde{\sigma}_{ij}$ and $\widetilde{m}_{nij}$ are tensors. Furthermore, a linear force-flux relation is stated within the Onsager theory, to satisfy Eq. (26):

$$J_i = \sum_j L_{ij} X_j\,. \tag{27}$$

Here, L_{ij} is a positiv-definite matrix of Onsager coefficients with the Onsager reciprocity relation, requiring symmetry of L_{ij}. Only equations of the same tensor rank are coupled over the reciprocity relation (Curie principle, [20]). This means, that all force terms of the same tensor rank superimpose each other and impact all fluxes of the same tensor rank, hence:

Scalar fluxes:

$$\begin{pmatrix} V_n^g \\ q_n^g \\ m_{nnn} \end{pmatrix} = \begin{pmatrix} \lambda_0 & \lambda_1 & \lambda_2 \\ \lambda_1 & \lambda_3 & \lambda_4 \\ \lambda_2 & \lambda_4 & \lambda_5 \end{pmatrix} \begin{pmatrix} \left[p_{sat}\left(T^l\right) - p^g - \sigma_{nn}\right] \\ \left[-\left(T^g - T^l\right) - \frac{\omega_3}{5}\,\mathrm{Pr}\,\sigma_{nn} - \frac{2\theta_2}{25}\,(\mathrm{Pr})^2\left(R_{nn} + \frac{\Delta}{3}\right)\right] \\ \left[-\frac{3\omega_2}{8}\sigma_{nn}\right] \end{pmatrix} \tag{28}$$

Vector fluxes:

$$\begin{pmatrix} \overline{\sigma}_{nk} \\ \overline{R}_{nk} \end{pmatrix} = \begin{pmatrix} \zeta_0 & \zeta_1 \\ \zeta_1 & \zeta_2 \end{pmatrix} \begin{pmatrix} \left[-\overline{V}_k - \frac{\omega_3}{5}\,\mathrm{Pr}\,\overline{q}_k - \frac{\omega_2}{2}\overline{m}_{nnk}\right] \\ \left[-\frac{2\theta_2}{25}\,(\mathrm{Pr})^2\,\overline{q}_k\right] \end{pmatrix} \tag{29}$$

Tensor fluxes:

$$\widetilde{m}_{nij} = -\kappa_0 \frac{\omega_2}{4}\widetilde{\sigma}_{ij} \tag{30}$$

For $\lambda_0 = \lambda_1 = \lambda_2 = 0$ one obtains the full set of phenomenological boundary conditions for a wall-gas interface, which are independent of evaporation as in Ref. [12]. The interface conditions (29-30), which consist of first order tensors (vectors) and second order tensors (matrices), respecitvely, have been fitted for a wall-gas interface in Ref. [12]. The fitting of (28) for evaporation at liquid-vapor interfaces shall be discussed in Sec. 3. In the following, the new evaporation boundary conditions (28-30) shall be referred to as PBC (phenomenological boundary conditions).

3. Determining the Onsager coefficients

3.1. Comparison to previous Macroscopic Boundary Conditions

The structure of PBC and MBC is very similar, the main difference lies in the values of the coefficients. As first step for determining the Onsager coefficients of the PBC (28-30), we aim to use the coefficients of the MBC in a way that all terms - except those where higher order moments, i.e., Δ, R_{ij}, m_{ijk} occur - agree to the MBC. This is justified due to the fact that the MBC predict effects in the Navier-Stokes regime very well. In the rarefied gas regime, however, their application seems to be more limited [11]. Since the higher moments are responsible for predicting a simplified Knudsen layer and also for rarefaction effects, a difference between PBC and MBC in these terms is desired. For a liquid-gas interface the matrix of Onsager coefficients of those boundary conditions with variables of zero tensor rank (28) assumes the dimension 3x3, in contrast to the wall-gas interface, where the matrix reads 2x2 [12]. Based on these thoughts, the following Onsager coefficients are suggested:

$$\lambda_0 = a\vartheta_2 \,, \tag{31}$$

$$\lambda_1 = b\left(-\frac{1}{2}\vartheta_2\right) \,, \tag{32}$$

$$\lambda_2 = c\left(-\frac{2}{5}\vartheta_2\right) \,, \tag{33}$$

$$\lambda_3 = d\left(\frac{1}{4}\vartheta_2 + 2\chi_2\right) \,, \tag{34}$$

$$\lambda_4 = e\left(\frac{1}{5}\vartheta_2 - \frac{2}{5}\chi_2\right) \,, \tag{35}$$

$$\lambda_5 = f\left(\frac{4}{25}\vartheta_2 + \frac{52}{25}\chi_2\right) \,, \tag{36}$$

with

$$\vartheta_2 = \sqrt{\frac{2}{\pi}}\frac{\vartheta}{2-\vartheta} \,, \qquad \chi_2 = \sqrt{\frac{2}{\pi}}\frac{\vartheta + \chi(1-\vartheta)}{2-\vartheta-\chi(1-\vartheta)} \quad .$$

To leave the coefficients adjustable, the factors $a...f$ have been introduced. For $a = b = ... = f = 1$, the PBC differ from the MBC, only in the higher order terms, see Appendix C. The boundary conditions (29-30) have been fitted for a wall-gas interface in Ref. [12] and shall not further be investigated here. To determine the coefficients $a...f$ by fitting to a DSMC solution, two evaporation problems will be discussed, for which analytical solutions for R13 with PBC can be obtained.

3.2. Simplification of R13 for 1-D Problems

As can be expected, the present PBC, just like the MBC, give less accurate results than methods, that solve the full Boltzmann Equation. The R13 equations and their corresponding interface and boundary conditions are simplifications of the Boltzmann Equation and carry fewer information.

The adjustable coefficients $a...f$ in (31-36) leave six degress of freedom to determine the Onsager coefficients. It is of interest, whether the simplification of R13 to the Boltzmann equation can be partly corrected by adjusting the Onsager coefficients. In this context we simplify the linear R13 equations for one-dimensional and steady systems and solve them for two problems, previously dicussed in [11]. Then, the new solutions are fitted to DSMC data.

All variables depend only on the location x. For the equilibrium rest state the saturation pressure of the liquid interface is set to $p_{sat}(T_0) = p_0$. We assume that the liquid temperature at the interface is controlled. Small pressure- or temperature changes are sufficient to drive evaporation or condensation. All equations are linear and dimensionless and describe the deviation to their equilibrium state. The simplified balance equations for mass, momentum and energy read

$$\frac{\partial v}{\partial x} = \frac{\partial \sigma}{\partial x} + \frac{\partial p}{\partial x} = \frac{\partial q}{\partial x} = 0\,. \tag{37}$$

After simple integration follows

$$v = V_0 = const\,, \quad p + \sigma = P_0 = const\,, \quad q_0 = Q_0 = const\,. \tag{38}$$

Hence, velocity and conductive heat flux are constant in the vapor phase. The normal components of the linear and non-dimensional constitutive equations for (7-9) obtain the form

$$\Delta = -\frac{8\mathrm{Kn}}{\mathrm{Pr}_\Delta}\frac{\partial q}{\partial x} = 0\,, \quad R_{nn} = -\frac{28}{5}\frac{\mathrm{Kn}}{\mathrm{Pr}_R}\frac{\partial q}{\partial x} = 0\,, \quad m_{nnn} = -\frac{3\mathrm{Kn}}{\mathrm{Pr}_M}\frac{\partial \sigma}{\partial x}\,, \tag{39}$$

with data to adjust between the molecule models from Table 1. The linear and non-dimensional equations for normal stress σ and conductive heat flux q_o become

$$\frac{6}{5}\mathrm{Kn}\frac{\partial^2 \sigma}{\partial x^2} = \frac{\sigma}{\mathrm{Kn}}\,, \tag{40}$$

$$\frac{\partial T_g}{\partial x} = -\frac{4q_0}{15\mathrm{Kn}} - \frac{2}{5}\frac{\partial \sigma}{\partial x}\,. \tag{41}$$

Integration yields

$$\sigma = A\sinh\left[\sqrt{\frac{5}{6}}\frac{x}{\mathrm{Kn}}\right] + B\cosh\left[\sqrt{\frac{5}{6}}\frac{x}{\mathrm{Kn}}\right]\,, \tag{42}$$

$$T_g = K - \frac{4q_0 x}{15\mathrm{Kn}} - \frac{2}{5}\sigma\,, \tag{43}$$

with A, B, K as constants of integration. There are 6 unknowns (V_0, P_0, Q_0, A, B, K), that must be determined for finding the solution. For evaporating interfaces, and by taking $\Delta = R = 0$ (39) into account, the normal boundary conditions (28) simplify to

$$V_o = \lambda_0\left[-P_0 + p_{sat}\left(T^l\right)\right] + \lambda_1\left[-\left(T_g - T_l\right) - \frac{\omega_3}{5}\mathrm{Pr}\,\sigma\right] - \lambda_2\frac{3\omega_2}{8}\sigma\,, \tag{44}$$

$$q_o = \lambda_1\left[-P_0 + p_{sat}\left(T^l\right)\right] + \lambda_3\left[-\left(T_g - T_l\right) - \frac{\omega_3}{5}\mathrm{Pr}\,\sigma\right] - \lambda_4\frac{3\omega_2}{8}\sigma\,, \tag{45}$$

$$\frac{6}{5}\mathrm{Kn}\left[\frac{\partial \sigma}{\partial x}\right] = \lambda_2\left[P_0 - p_{sat}\left(T^l\right)\right] + \lambda_4\left[\left(T_g - T_l\right) + \frac{\omega_3}{5}\mathrm{Pr}\,\sigma\right] + \lambda_5\frac{3\omega_2}{8}\sigma\,, \tag{46}$$

with $V_o = n_k V_k$ and $q_o = q_k n_k$.

3.3. Problem I: Vapor layer between two liquid reservoirs

In the first problem for fitting the coefficients $a...f$, and also for getting an insight into the Knudsen layers, we consider one-dimensional, steady-state heat- and mass transfer within a vapor phase in between two liquid reservoirs with controlled temperature on liquid side of the liquid-vapor interfaces. The configuration has been discussed in [11] and shall be outlined only briefly here.

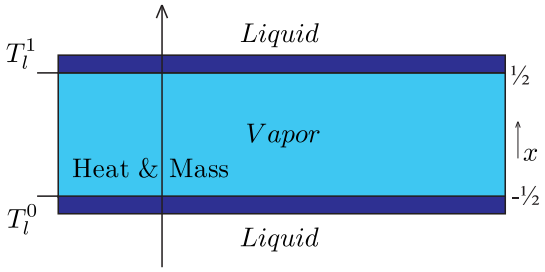

Figure 1. System I: Vapor phase between two liquid reservoirs.

The interfaces are located at $x = \pm\frac{1}{2}$ with the normal vector n pointing from liquid into vapor and the superscripts 0 for $x = -\frac{1}{2}$ and 1 for $x = \frac{1}{2}$, i.e., $V_0^0 = -V_0^1 = V_0$. Driving force for evaporation and condensation is the temperature difference between T_l^0 and T_l^1. The required six equations are found by evaluating the boundary conditions (28) at both interfaces. For evaluation of the equations, it is convenient to take both the sums and the differences at both interfaces. For the three sums follows

$$P_o = \frac{1}{2}\left(p_{sat}^0(T_l^0) + p_{sat}^0(T_l^1)\right) , \tag{47}$$

$$\left(T_l^0 + T_l^1\right) - \left(T_g^0 + T_g^1\right) = 0 , \tag{48}$$

$$\sigma^0 = -\sigma^1 . \tag{49}$$

Stress profile Eq. (42) and temperature profile, Eq. (43), follow as

$$\sigma = A \sinh\left[\sqrt{\frac{5}{6}}\frac{x}{\mathrm{Kn}}\right] , \tag{50}$$

$$T_g = \frac{(T_l^0 + T_l^1)}{2} - \frac{4q_0 x}{15\mathrm{Kn}} - \frac{2}{5} A \sinh\left[\sqrt{\frac{5}{6}}\frac{x}{\mathrm{Kn}}\right] . \tag{51}$$

The three differences of the normal boundary conditions form a linear system for V_0, Q_0 and A as

$$V_0 = \frac{1}{2}\begin{pmatrix} \lambda_0\left[p_{sat}\left(T_l^0\right) - p_{sat}\left(T_l^1\right)\right] \\ +\lambda_1\left[-\frac{4q_0}{15\mathrm{Kn}} + \left(T_l^0 - T_l^1\right) + \left(\frac{2\omega_3}{5}\mathrm{Pr} - \frac{4}{5}\right) A \sinh\left[\frac{1}{2}\sqrt{\frac{5}{6}}\frac{1}{\mathrm{Kn}}\right]\right] \\ +\frac{3\omega_2}{4}\lambda_2 A \sinh\left[\frac{1}{2}\sqrt{\frac{5}{6}}\frac{1}{\mathrm{Kn}}\right] \end{pmatrix} , \tag{52}$$

$$Q_0 = \frac{1}{2}\begin{pmatrix} \lambda_1\left[p_{sat}\left(T_l^0\right) - p_{sat}\left(T_l^1\right)\right] \\ +\lambda_3\left[-\frac{4q_0}{15\mathrm{Kn}} + \left(T_l^0 - T_l^1\right) + \left(\frac{2\omega_3}{5}\mathrm{Pr} - \frac{4}{5}\right) A \sinh\left[\frac{1}{2}\sqrt{\frac{5}{6}}\frac{1}{\mathrm{Kn}}\right]\right] \\ +\lambda_4\frac{3\omega_2}{4} A \sinh\left[\frac{1}{2}\sqrt{\frac{5}{6}}\frac{1}{\mathrm{Kn}}\right] \end{pmatrix} , \tag{53}$$

$$A = \frac{1}{\frac{12}{5}\sqrt{\frac{5}{6}}\cosh(\frac{1}{2}\sqrt{\frac{5}{6}}\frac{1}{\mathrm{Kn}})} \begin{pmatrix} \lambda_4\left[\frac{4q_o}{15\mathrm{Kn}} + (T_l^1 - T_l^0) + \left(\frac{4}{5} - \frac{2\omega_3}{5}\,\mathrm{Pr}\right) A\sinh\left[\frac{1}{2}\sqrt{\frac{5}{6}}\frac{1}{\mathrm{Kn}}\right]\right] \\ -\lambda_5\frac{3\omega_2}{4} A\sinh\left[\frac{1}{2}\sqrt{\frac{5}{6}}\frac{1}{\mathrm{Kn}}\right] + \lambda_2\left[p_{sat}\left(T_l^1\right) - p_{sat}\left(T_l^0\right)\right] \end{pmatrix} . \quad (54)$$

Here, A is the amplitude of the Knudsen layer. We refrain from showing the solution but will only show results from the inversion in the figures. For the linear NSF-Onsager boundary conditions, see Appendix D, one finds

$$V_0 = \frac{r_{22}}{r_{11}r_{22} - r_{12}r_{12}}\frac{1}{\sqrt{2\pi}}\frac{1}{2}\left(p_{sat}^0(T_l^0) - p_{sat}^1(T_l^1) + \frac{r_{12}}{r_{22}}\left(\frac{4Q_0}{15\mathrm{Kn}} + T_l^1 - T_l^0\right)\right) , \quad (55)$$

$$q_0 = \frac{1}{r_{22}}\frac{1}{2}\left(\frac{1}{\sqrt{2\pi}}\left(-\frac{4Q_0}{15\mathrm{Kn}} + T_l^0 - T_l^1\right) - 2r_{12}V_0\right) , \qquad A = 0 . \quad (56)$$

The given solution for NSF is a simplification for $\chi = \vartheta = 1$, see Appendix D. For the NSF-Onsager coefficients r_{11}, r_{12} and r_{22} the Onsager matrix (D.2) or the corrected Onsager matrix (D.3) can be used. The solution of the MBC for this system can be found in [11]. Results shall be compared in Sec. 3.5 and 3.6.

3.4. Problem II: Evaporation in Half-Space Problem

In the half space problem, a liquid interface evaporates into the equilibrium state, as discussed previously in Ref. [11]. Driving force is the prescribed pressure p_∞ far away from the interface, see Fig. 2.

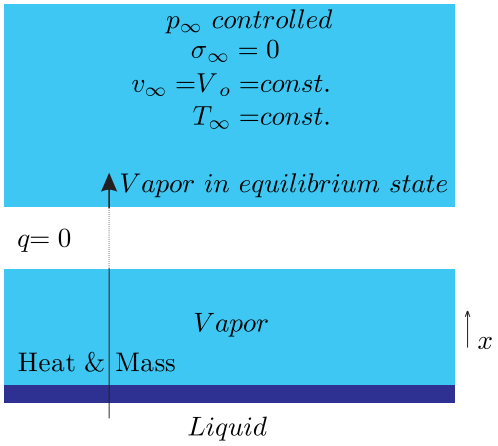

Figure 2. System II: Half-space problem.

The six unknowns are found by considering evaporation boundary conditions on one side and constant velocity $v_\infty = V_0$, pressure $p_\infty = P_0$ and temperature T_∞ far away from the interface. For reaching constant pressure p_∞ and due to the momentum balance (38), it is necessary to set the normal stress far away from the interface to $\sigma_\infty = 0$. Moreover, conductive heat flux q_0 is set to zero as well. With T_∞ prescribed, one finds the constant K. For (50,51) it follows

$$\sigma(x) = A\exp\left[-\sqrt{\frac{5}{6}}\frac{x}{\mathrm{Kn}}\right] , \quad (57)$$

$$T(x) = T_\infty - \frac{2}{5}\sigma(x) . \quad (58)$$

Table 2. Factors to adjust the Onsager coefficients of the PBC for the standard temperature profile.

	a	b	c	d	e	f
PBC standard profile	1.02	0.96	1.30	0.94	0.50	1.20

Evaluating the boundary conditions (28) at the interface between liquid and vapor leads to

$$v_\infty = \lambda_0 \left[p_{sat}\left(T_l\right) - p_\infty\right] + \lambda_1 \left(T_l - T_\infty\right) + \left(\lambda_1 \left(\frac{2}{5} - \frac{\omega_3}{5}\,\mathrm{Pr}\right) - \lambda_2 \frac{3\omega_2}{8}\right) A\,, \tag{59}$$

$$0 = \lambda_1 \left[p_{sat}\left(T_l\right) - p_\infty\right] + \lambda_3 \left(T_l - T_\infty\right) + \left(\lambda_3 \left(\frac{2}{5} - \frac{\omega_3}{5}\,\mathrm{Pr}\right) - \lambda_4 \frac{3\omega_2}{8}\right) A\,, \tag{60}$$

$$0 = \lambda_2 \left[p_{sat}\left(T_l\right) - p_\infty\right] + \lambda_4 \left(T_l - T_\infty\right) + \left(\lambda_4 \left(\frac{2}{5} - \frac{\omega_3}{5}\,\mathrm{Pr}\right) - \lambda_5 \frac{3\omega_2}{8} - \frac{6}{5}\sqrt{\frac{5}{6}}\right) A\,. \tag{61}$$

For Navier-Stokes-Fourier out of Eq. (D.1) follows

$$v_\infty = \frac{p_{sat}(T_l) - p_\infty}{\sqrt{2\pi} r_{11}}\,, \tag{62}$$

$$v_\infty = \frac{1}{\sqrt{2\pi}} \frac{T_l - T_\infty}{r_{21}}\,. \tag{63}$$

With prescribed pressure p_∞ and by setting $p_{sat}(T_l) - p_\infty = \Delta p$ and $T_l - T_\infty = \Delta T$, there are three unknowns v_∞, T_∞ and A, which can be calculated with (59-61) for PBC and (62,63) for NSF. The solution for the MBC can again be found in Ref. [11]. Note that for NSF A is zero and the given two equations are sufficient.

Ytrehus, who discussed the half space problem in Ref. [15], proposed dimensionless ratios in which the prescribed pressure p_∞ is eliminated. The ratios which make it easy to compare different models, e.g., Maxwell molecules, BGK, Navier-Stokes-Fourier etc. read:

$$\alpha_p = \frac{p_{sat}\left(T_l\right) - p_\infty}{\frac{v_\infty}{\sqrt{2}}}\,, \tag{64}$$

$$\alpha_\theta = \frac{T_l - T_\infty}{\frac{v_\infty}{\sqrt{2}}}\,. \tag{65}$$

Note, that (59-63) and therefore also (64,65) are independent of the Knudsen number.

3.5. Fitting of the Onsager Coefficients: Standard Temperature Profile

The ratios (64,65) from Problem II together with DSMC data for Problem I shall be used to fit the coefficients $a...f$ in (31-36). The temperatures and saturation pressures at the liquid boundaries are given as $T_l^0 = p_{sat}(T_l^0) = 1.05$ and $T_l^1 = p_{sat}(T_l^1) = 0.95$. All results in the following are based on full evaporation and fully diffusive reflection, by setting the evaporation and accommodation coefficients $\vartheta = \chi = 1$. Maxwell molecules are considered, and their data is taken out of Table 1. In Table 2 factors for the Onsager coefficients, used in Eqs. (31-36), which have been found by trial and error are suggested to adjust the PBC, Eqs. (28), for best fit. The results of the new PBC are compared with the previously derived evaporation boundary conditions (MBC) and also with Navier-Stokes-Fourier solutions. NSF is based on Onsager boundary conditions as well and uses the Onsager matrix (D.2) or the corrected Onsager matrix (D.3).

Ytrehus used a moment method to solve the half space problem with high precision [15] and his results are used here as reference. Ytrehus' ratios α_p, α_θ (64,65) have been calculated for PBC, MBC,

Preprints (www.preprints.org) | NOT PEER-REVIEWED | Posted: 18 July 2018 doi:10.20944/preprints201807.0327.v1

Peer-reviewed version available at Entropy 2018, 20, 680; doi:10.3390/e20090680

Table 3. Solutions for Ytrehus' ratios and percentual deviation to Ytrehus' solution for the standard temperature profile.

	α_p	% to Ytrehus	α_θ	% to Ytrehus
PBC standard profile	2.0956	1.40	0.4875	10.02
MBC	2.1097	0.74	0.4894	10.44
NSF	1.9940	6.18	0.4431	-
NSF corrected	2.1254	-	0.4472	0.93
Ytrehus	2.1254	-	0.4431	-

NSF and corrected NSF. Together with the percentual deviation to Ytrehus' solution they are given in Table 3.

By trial and error fitting of the Onsager coefficients it was not possible to achieve superior agreement between PBC and DSMC for Problem I (Sec. 3.3) and proper results for Ytrehus' ratios (64,65) at the same time. Forcing good agreement between Ytrehus' solution of the half space problem and PBC regarding the dimensionless ratios showed significant decrease in agreement between PBC and DSMC for Problem I. The fittings that are chosen here are compromises between Problem I and Problem II but with strong emphasis on achieving proper results for Problem I, which means proper agreement with DSMC results.

Fig. 3 shows temperature and normal stress profiles for Kn $= 0.078$. R13 with PBC (solid, purple) and MBC (solid, red) are in good agreement with DSMC (green, dashed). The amplitude of the Knudsen layer A is zero for NSF (black, dashed) and corrected NSF (blue, dashed). As a result both NSF solutions slightly deviate from DSMC close to the boundaries. $A = 0$ removes the last term in (51) and therefore leads to a linear function. In Problem I, NSF is not able to predict normal stress at all, see Eqs. (55,56).

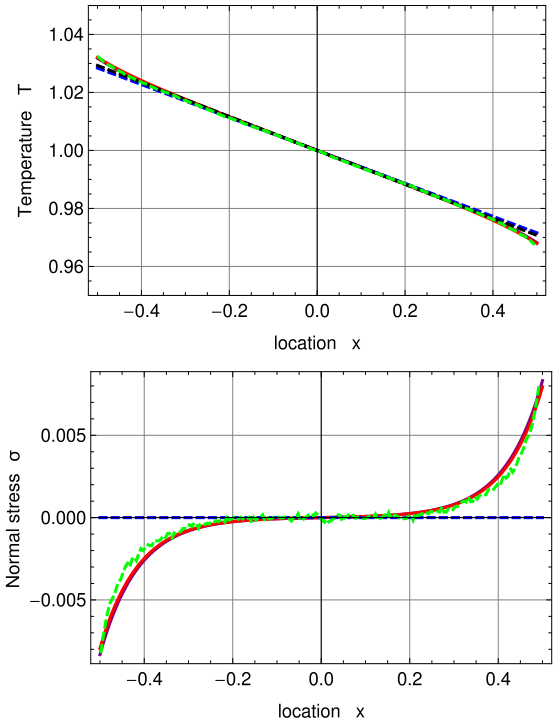

Figure 3. Temperature and normal stress profiles for Kn $= 0.078$ with $\Delta T = 0.05$ and $\Delta p = 0.05$: DSMC (symmetrized; green, dashed), R13 with PBC (purple), R13 with MBC (red), corrected NSF (blue, dashed), uncorrected NSF (black, dashed).

In Fig. 4 temperature and normal stress profiles are illustrated for Kn $= 0.235$. Both sets of boundary conditions for R13 reconstruct the DSMC results well but slightly underpredict the Knudsen layers both for temperature and normal stress. For the temperature profile they are in better agreement with DSMC than the two NSF solutions. For both Kn $= 0.078$ and Kn $= 0.235$ one notes the significant temperature jumps at the boundaries.

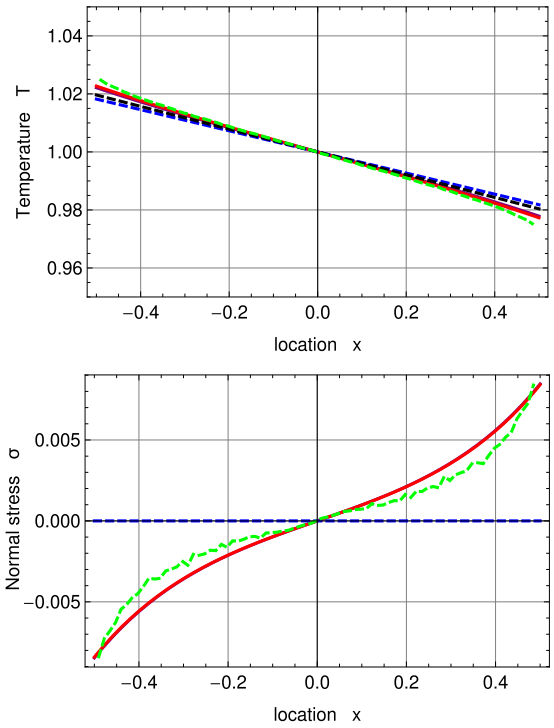

Figure 4. Temperature and normal stress profiles for Kn $= 0.235$ with $\Delta T = 0.05$ and $\Delta p = 0.05$: DSMC (symmetrized; green, dashed), R13 with PBC (purple), R13 with MBC (red), corrected NSF (blue, dashed), uncorrected NSF (black, dashed).

Additionally to temperature and normal stress profiles, we seek to get insight into the three integration constants velocity V_0, heat conduction q_0 and Knudsen Layer amplitude A, depending on the Knudsen number. The three variables are plotted over Kn $= \{0, ..., 1\}$ in Fig. 5.

The sign of velocity V_0 and heat conduction q_0 are positive. That is, mass and conductive heat flux are transferred from warm to cold, which means they are transported at $x = -\frac{1}{2}$ into the system via evaporation and due to steady state, the same amount of mass and conductive heat is transported at $x = \frac{1}{2}$ out of the system into the colder reservoir via condensation .

The purple, large, dashed line represents R13 with PBC for $a = b... = f = 1$, see Appendix C. Although there are differences in the higher order terms between PBC and MBC, if the adjustable coefficients are set to unity, the order of magnitude of the maximum deviation between the two models is with $\pm 10^{-7}$ very small, i.e., at first glance, both plots appear to be identical.

R13 with PBC shows very good agreement with DSMC for V_0 and q_0 for all Knudsen numbers. The PBC results for normal stress are better than those of MBC for Kn < 0.3. For higher Knudsen numbers both PBC and MBC fail to predict σ in precise agreement with DSMC. Again normal stress can not be predicted by NSF.

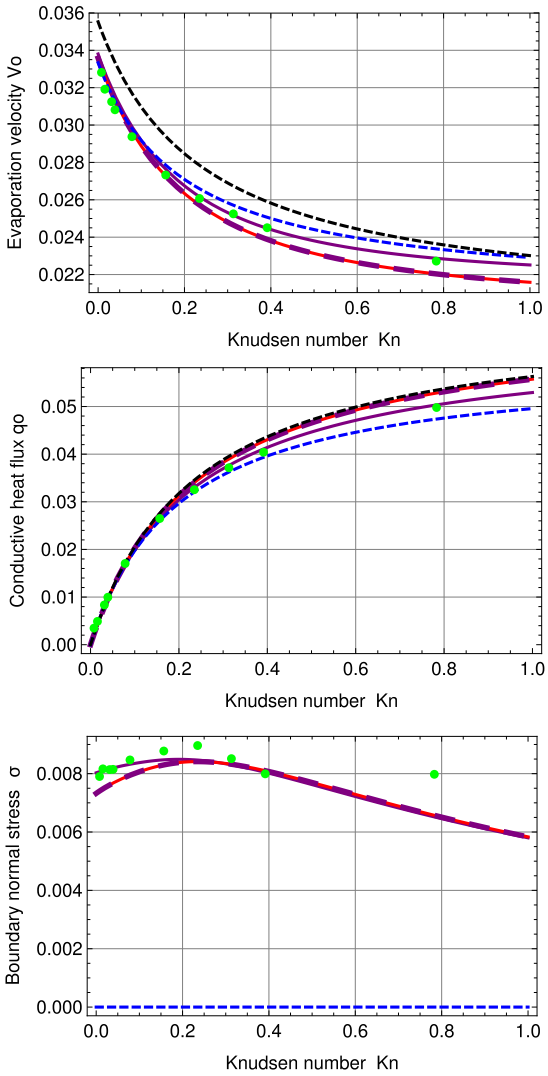

Figure 5. Evaporation velocity V_0, conductive heat flux q_0 and boundary normal stress σ_0 for standard temperature profile: DSMC (green, dots), R13 with PBC (purple), R13 with PBC: $a...f = 1$ (purple, large, dashed), R13 with MBC (red), corrected NSF (blue, dashed), uncorrected NSF (black, dashed).

Interestingly for this PBC fit, Ytrehus' ratios are similar to those of the MBC, i.e., 1.4% (PBC) and 0.74% (MBC) deviation for α_p and 10.02% (PBC) and 10.44% (MBC) for α_θ, see Table 3. Corrected NSF is under 1% deviation for both ratios. Uncorrected NSF shows zero deviation for α_θ and 6.18% for α_p. For Knudsen numbers larger than Kn $= 0.235$ the deviation between DSMC and PBC becomes slightly larger for the temperature profile and stays similar for the normal stress profile. The temperature jump at the boundaries increases with increasing Knudsen number.

3.6. Fitting of the Onsager Coefficients: Inverted Temperature Profile

By adjusting the values for ΔT and Δp, it can be shown that the sign of the conductive heat flux q_0 switches. This leads to an inverted temperature profile as depicted below. The negative sign of q_0 indicates conductive heat transport from $x = \frac{1}{2}$ to $x = -\frac{1}{2}$, see Fig. 1. Though, the second law is not violated, since the overall heat transport is given with $Q = \rho V_0 h + q_0$ and the advective term $\rho V_0 h$ is dominant. Hence, the overall heat Q is transported from hot to cold as expected. One notes, that due to the reversed sign of the conductive heat flux, the necessary vaporization enthalpy is partly provided by the colder boundary. The liquid temperatures at the boundaries are set to $T_l^0 = 1.01$ and $T_l^1 = 0.99$ and the respective saturation pressures to $p_{sat}(T_l^0) = 1.0752$ and $p_{sat}(T_l^1) = 0.9248$. Therefore the

Table 4. Factors to adjust the Onsager coefficients of the PBC for the inverted profile.

	a	b	c	d	e	f
PBC inverted profile	0.983	0.83	1.30	0.87	0.50	1.20

Table 5. Solutions for Ytrehus' ratios and percentual deviation to Ytrehus' solution for inverted profile.

	α_p	% to Ytrehus	α_θ	% to Ytrehus
PBC inverted profile	2.1352	0.46	0.4657	5.11
Ytrehus	2.1254	-	0.44311	-

evaporating material of the system is different to the one considered for the standard temperature profile. The small temperature difference between hot and cold boundaries and the large difference between the saturation pressures allows for a temperature jump large enough to reverse the sign of the conductive heat flux.

By fitting with trial and error, it was not possible to achieve good fits for the standard and inverted temperature profiles at the same time. We believe, this is due to the evaporating material being different between the standard and inverted cases, since the saturation pressures are different. Therefore we present a fitting for the adjustable factors within the PBC for the inverted case, which is given in Table 4.

The ratios α_p,α_θ as well as the percentual deviation to Ytrehus' solution are presented in Table 5.

The temperature and stress profiles for Kn $= 0.078$ are given in Fig. 6. As comparison to the new fitting, a PBC solution, which uses the previous coefficients, is given as well (purple, dashed). R13 with PBC and MBC both overpredict the Knudsen layer at the interfaces. For the temperature profile, corrected NSF shows the best agreement with DSMC here. Normal stress is predicted well for PBC and MBC and is again zero for NSF.

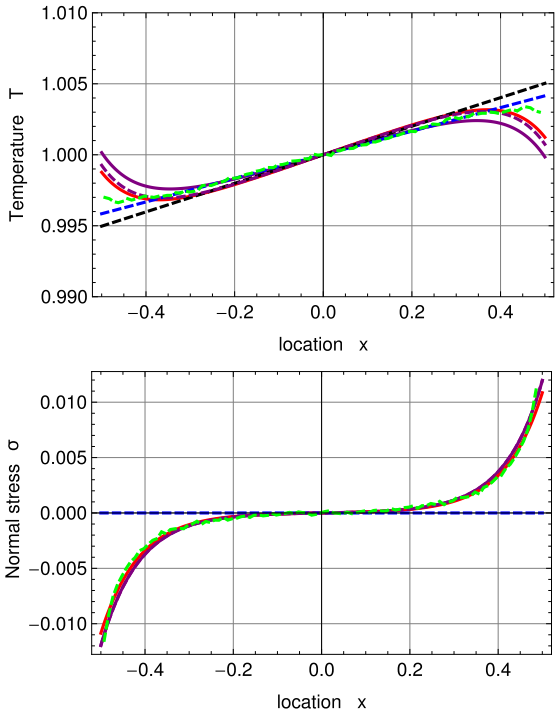

Figure 6. Inverted temperature and normal stress profiles for Kn $= 0.078$ with $\Delta T = 0.01$ and $\Delta p = 0.075$: DSMC (symmetrized; green, dashed), R13 with PBC (purple), R13 with PBC and previous fitting (purple, dashed), R13 with MBC (red), corrected NSF (blue, dashed), uncorrected NSF (black, dashed).

For Kn $= 0.235$ the overprediction of the R13 boundary conditions becomes so large, that the profiles are not inverted anymore, as shown in Fig. 7. Note, that it is possible to "turn" the PBC temperature profile to match the DSMC results, however this leads to worse results for other plots. In this case, MBC shows slightly better results for temperature and normal stress profiles than PBC.

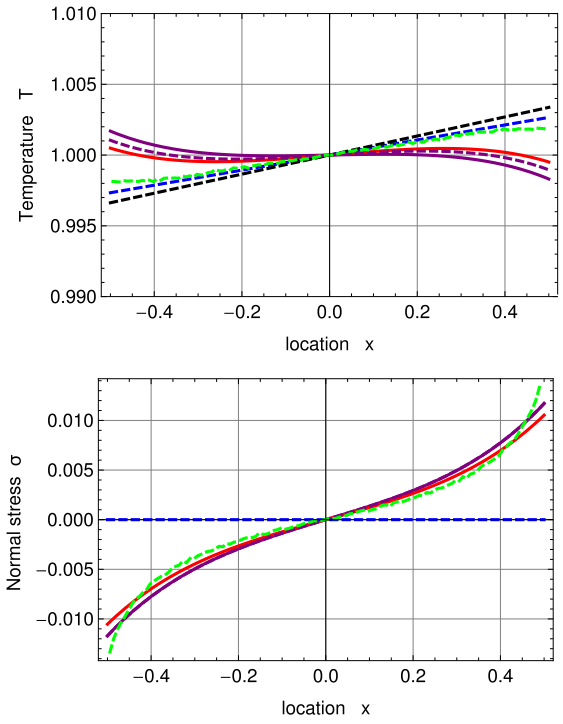

Figure 7. Inverted temperature and normal stress profiles for Kn $= 0.235$ with $\Delta T = 0.01$ and $\Delta p = 0.075$: DSMC (symmetrized; green, dashed), R13 with PBC (purple), R13 with PBC and previous fitting (purple, dashed), R13 with MBC (red), corrected NSF (blue, dashed), uncorrected NSF (black, dashed).

Fig. 8 illustrates velocity, conductive heat flux and normal boundary stress for the inverted temperature profile. The purple, large, dashed line represents R13 with PBC and $a = b... = f = 1$. With an order of magnitude of $\pm 10^{-7}$, in the deviation to the MBC solution, the results of both models are again very similar, see also Fig. 5.

For evaporation velocity V_0 and conductive heat flux q_0, R13 with PBC is in very good agreement with DSMC. In comparison to the standard temperature profile, the normal boundary stress of the PBC starts to differ from DSMC earlier, i.e., for Kn > 0.1. Corrected NSF is in surprisingly good agreement with DSMC for Kn < 0.3 but fails to predict normal boundary stress. Except for temperature and normal stress profiles for Kn $= 0.235$, R13 with PBC shows the best agreement with DSMC compared to all discussed models here.

Preprints (www.preprints.org) | NOT PEER-REVIEWED | Posted: 18 July 2018 doi:10.20944/preprints201807.0327.v1

Peer-reviewed version available at Entropy 2018, 20, 680; doi:10.3390/e20090680

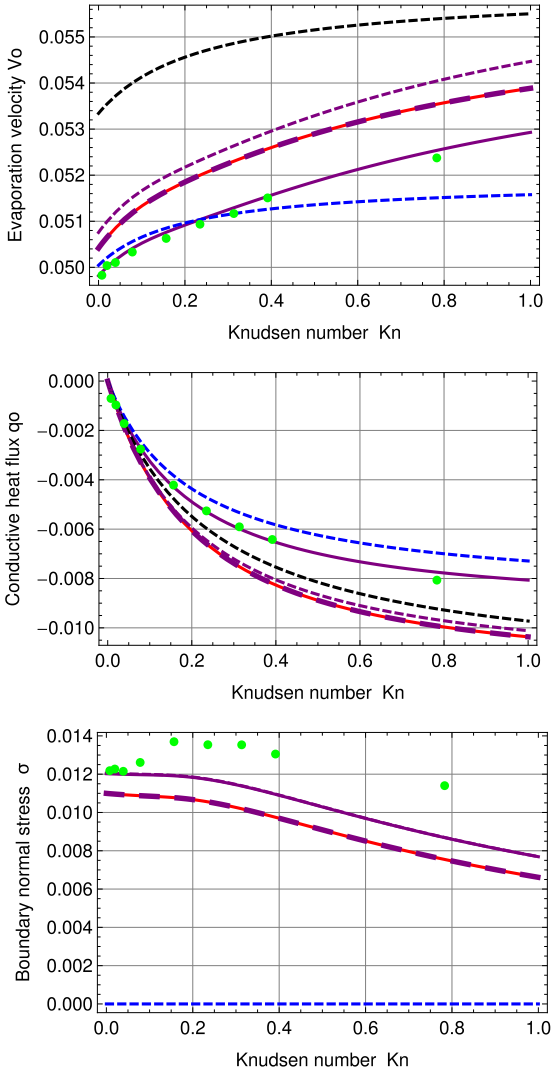

Figure 8. Evaporation velocity V_0, conductive heat flux q_0 and boundary normal stress σ_0 for inverted temperature profile: DSMC (green, dots), R13 with PBC (purple), R13 with PBC: $a...f = 1$ (purple, large, dashed), R13 with PBC and previous fitting (purple, dashed), R13 with MBC (red), corrected NSF (blue, dashed), uncorrected NSF (black, dashed). Note: For σ, the purple, dashed line is underneath the purple, solid line.

One notes, that for this PBC fitting, the deviations of 5.11% in α_θ and 0.46% in α_p to Ytrehus' solution become smaller than for the standard profile.

3.7. Impact of evaporation and accommodation coefficients

To gain a better understanding of the impact of evaporation and accommodation coefficients, the PBC shall be tested for the standard temperature profile of the previously discussed problem and a variety of ϑ, χ. Fig. 9 illustrates solutions of the PBC for Problem I (Sec. 3.3) together with the fitting from Table 2 and Kn $= 0.078$. The plots are based on $\chi = 0.1$ (Green), $\chi = 0.5$ (Red), $\chi = 1$ (Blue), $\vartheta = 0.1$ (solid), $\vartheta = 0.5$ (dashed) and $\vartheta = 1$ (large dashed).

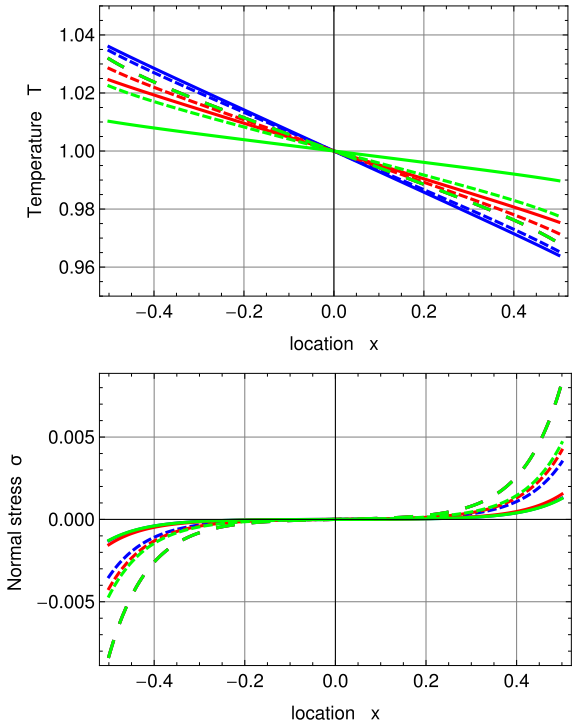

Figure 9. PBC temperature and normal stress profiles for Kn $= 0.078$ and various evaporation and accommodation coefficients: $\chi = 0.1$ (Green), $\chi = 0.5$ (Red), $\chi = 1$ (Blue), $\vartheta = 0.1$ (solid), $\vartheta = 0.5$ (dashed), $\vartheta = 1$ (large, dashed). Note: For $\vartheta = 1$, the green, large dashed curve represents the solutions of all three χ.

For $\vartheta = 1$, the solutions are independent of χ. Since the evaporation coefficient is defined through the condensation coefficient, this may be explained due to the fact that for the condensation coefficient being unity, no reflection occurs, all vapor molecules hitting the liquid interface are condensed. The largest temperature jump between gas and boundary is found for $\vartheta = 0.1$ and $\chi = 0.1$ and the smallest for $\chi = 1$.

The stress profile seems to be dependent, mainly on the evaporation coefficient. The accommodation coefficient has only a small impact for $\vartheta = 0.5$. The largest stress can be found for $\vartheta = 1$. Evaporation velocity V_0, conductive heat flux q_0 and boundary normal stress σ for various values of ϑ and χ are depicted in Fig. 10.

Preprints (www.preprints.org) | NOT PEER-REVIEWED | Posted: 18 July 2018 doi:10.20944/preprints201807.0327.v1

Peer-reviewed version available at Entropy 2018, 20, 680; doi:10.3390/e20090680

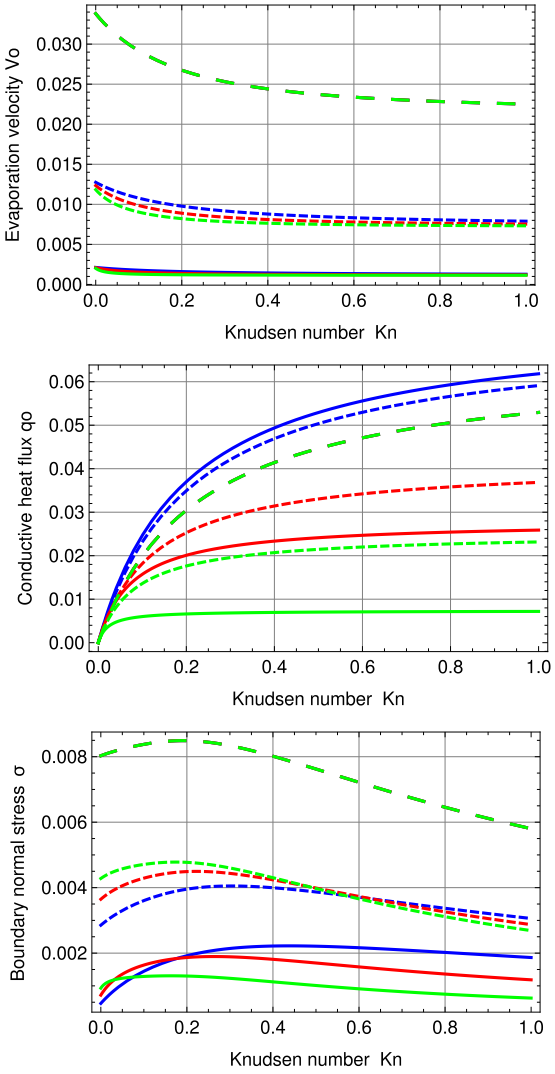

Figure 10. PBC evaporation velocity V_0, conductive heat flux q_0 and boundary normal stress σ_0 for standard temperature profile and various evaporation and accommodation coefficients: $\chi = 0.1$ (Green), $\chi = 0.5$ (Red), $\chi = 1$ (Blue), $\vartheta = 0.1$ (solid), $\vartheta = 0.5$ (dashed), $\vartheta = 1$ (large, dashed). Note: For $\vartheta = 1$, the green, large dashed curve represents the solutions of all three χ.

The results of V_0 seem to be almost independent of χ, except for $\vartheta = 0.5$, where χ has a small impact. Interestingly, χ has a large influence on q_0 and σ, particularly for $\vartheta = 0.1$.

3.8. Notes on the meaning of the individual Onsager coefficients of the normal fluxes

The fittings used in the Tables 2 and 4 are based on a trial and error procedure, in which the factors $a...f$ within the Onsager coefficients (31-36) are individually adjusted. Due to symmetry of the Onsager matrix, six independent parameters need to be determined. The tuning of the Onsager coefficients one by one gives an insight into their respective impact. However, one notes, that due to the coupling within the Onsager matrix in Eq. (28), the individual Onsager coefficient impacts multiple fluxes. The following is an attempt to highlight some trends, which were observed during the fitting procedure.

Since λ_0 appears only in the equation for the normal velocity, it has a strong impact on V_0 and no impact on the conductive heat flux q_0. Apparently it has no impact on the boundary normal stress σ. Temperature and stress profiles appear to be independent of λ_0 as well. The coefficient λ_1 has a big impact on V_0 and q_0 and a small impact on σ. It has a major impact on the temperature profile and a

Table 6. Derivation of boundary conditions by adjusting the Onsager coefficients

	Evaporation/condensation	Wall with energy transfer	Inflow/outflow
λ_0	$0.975\vartheta_2$	0	$1/10^{-5}$
λ_1	$-0.4375\vartheta_2$	0	0
λ_2	$-0.4\vartheta_2$	0	0
λ_3	$2.2\chi_2$	$1.744\vartheta_2$	$1/10^{-5}$
λ_4	$-0.28\chi_2$	$-1.744\vartheta_2$	0
λ_5	$2.184\chi_2 + 0.28\vartheta_2$	$2\vartheta_2$	0
ζ_0	χ_2 (Not fitted)	$0.9143\vartheta_2$	1.0 (Not fitted)
ζ_1	$-\chi_2$ (Not fitted)	$-0.9143\vartheta_2$	1.0 (Not fitted)
ζ_2	$13\chi_2$ (Not fitted)	ϑ_2	1.0 (Not fitted)
κ_0	$2\chi_2$ (Not fitted)	$2\vartheta_2$ (Not fitted)	1.0 (Not fitted)

smaller impact on the stress profile. λ_2 strongly influences V_0 and σ and very slightly q_0. Since λ_2 does not appear in the equation for q_0, this is expected. It has an impact on temperature and stress profiles but with clear emphasis on the stress profile.

The coefficient λ_3 seems to play a key role in the fitting. Even though it appears only in the equation for q_0, it has not only a strong impact on the magnitude and slope of q_0, but also on those of V_0 and σ. Regarding the profiles, λ_3 seems to impact mainly the temperature and only very slightly the stress. The Onsager coefficient λ_4 mainly impacts σ, but also V_0, q_0 and both profiles, with stronger impact on the stress profile, as expected. λ_5 appears only in the equation for the normal component of the higher moment m_{nnn}. The coefficient has a strong impact on σ, a medium impact on V_0 and no impact on q_0. It influences the stress profile significantly and the temperature profile slightly.

After these dependencies were established, several rounds of fitting were done, until a reasonable fitting was obtained.

4. Evaporation in Numerical Two-Dimensional Steady-State Simulation

4.1. R13 with Onsager Boundary Conditions in Numerical Simulation

It shall be shown that the applicability of R13 with PBC (Phenomenological Boundary Conditions) is not limited to one-dimensional systems. The code of Torrilhon & Sarna [21], written in C++, is used in this section to solve the R13 equations with PBC for evaporation. As comparison, simplified NSF (Navier-Stokes-Fourier) is solved with the same program. Torrilhon & Sarna's code allows for generic implementation of macroscopic transport equations. The numerical solver relies on a discontinuous Galerkin (DG) method which utilizes finite elements to discretize the system. Here the code is extended by implementing the evaporation boundary conditions previously derived in Sec. 3 and also simplified Onsager boundary conditions for NSF.

The PBC for R13, given in Eqs. (28-30), are adjusted by using data for Maxwell molecules out of Table 1. The liquid phase is not solved and therefore can be treated in the same manner as a wall, which allows for mass transfer. Adjustment of the Onsager coefficients allows to derive other boundary conditions, such as wall with energy transfer or inflow/outflow. Table 6 gives an overview about these modifications.

For an adiabatic wall (fully specular reflective) all Onsager coefficients are set to zero, which leads to $v_n^g = q_n^g = m_{nnn} = \overline{\sigma}_{nk}^g = \overline{R}_{nk} = \widetilde{m}_{nij} = 0$. The Onsager coefficients for a wall with energy transfer are taken from Ref. [12]. The adjustable coefficients within the Onsager coefficients for the different boundaries are already implemented in Table 6.

Note: Compared to Sec. 3.1, a slightly different fitting is used here. Additionally, the coefficients used in $\lambda_0, ..., \lambda_5$ are based on adjustments as in Problem I (Sec. 3.3), however different definitions of the Knudsen number between DSMC and R13 were used. Therefore a small error is introduced here.

Preprints (www.preprints.org) | NOT PEER-REVIEWED | Posted: 18 July 2018 doi:10.20944/preprints201807.0327.v1

Peer-reviewed version available at Entropy 2018, 20, 680; doi:10.3390/e20090680

Table 7. Overview of input parameters for the boundary conditions

	Evaporation/condensation	Wall with energy transfer	Inflow/outflow
p_{sat}	p_{evap}	$-$	$\pm p_{flow}$
T_l	T_{evap}	T_w	T_{flow}

The coefficients in $\zeta_0, ..., \zeta_2$ and κ_0 are not fitted and set to unity. The adjustable coefficients for a wall with energy transfer $\lambda_3, ..., \lambda_5$ and $\zeta_0, ..., \zeta_2$ are taken from Ref. [12] and κ_0 is set to unity here. Depending on the boundary, different pressures and temperatures are assumed, as depicted in Table 7.

For a detailed description of the numerical solution, see [21].

4.2. Navier-Stokes-Fourier with Onsager Boundary Conditions in Numerical Simulation

For obtaining a comparison to the R13 solutions for two-dimensional systems, the Navier-Stokes-Fourier equations together with Onsager boundary conditions for evaporation/condensation are used here. For $\chi = \vartheta = 1$ and considering one-dimensional geometry, evaporation boundary conditions for NSF are given in Appendix D, see. (D.1). For 2- and 3-dimensional geometries an additional boundary condition is found in Ref. [11] and reads

$$\overline{\sigma}^g_{nk} = -\frac{\vartheta + \chi(1-\vartheta)}{2 - \vartheta - \chi(1-\vartheta)} \sqrt{\frac{2}{\pi RT}} \left(p\overline{v}^g_k + \frac{1}{5}\overline{q}^g_k \right) . \tag{66}$$

Note that Eqs. (D.1) are simplified equations for 1-D geometry. Again by considering $\chi = \vartheta = 1$ and after full linearization and non-dimensionalization, Eq. (66) becomes

$$\overline{\sigma}^g_{nk} = -\sqrt{\frac{2}{\pi}} \left(\overline{v}^g_k + \frac{1}{5}\overline{q}^g_k \right) . \tag{67}$$

4.3. Numerical Solutions for Two-Dimensional Channel-Flow with four Evaporating Cylinders

The system of interest for the two-dimensional, steady-state simulation is a channel with four evaporating cylinders, which is discretized as depicted in Fig. 11.

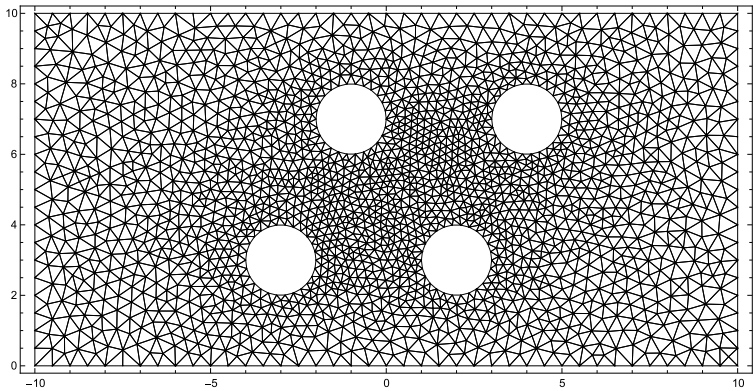

Figure 11. Grid of two-dimensional channel-flow with four evaporating cylinders.

The left boundary is the inlet of the channel flow and the right boundary is the outlet. Top and bottom are walls, which allow energy transfer. The cylinder walls use evaporation boundary conditions given by (28-30) with Table 6 for R13 and (67, D.1, D.3) for NSF.

The input parameters, which are given in Table 8, are non-dimensional and describe the deviation to equilibrium. They are chosen in a way, that evaporation at the cylinders can be observed clearly.

The plots in Fig. 12 show pressure contours, superimposed by velocity streamlines, for R13 and NSF, for the three Knudsen numbers: Kn $= \{0.1, 0.5, 1\}$.

Table 8. Input parameters for two-dimensional channel flow with four evaporating cylinders.

	Evaporation/condensation	Wall with energy transfer	Inflow/outflow
p_{sat}	$p_{evap} = 0.2$	–	$\pm p_{flow} = 0.1$
T_l	$T_{evap} = 0.2$	$T_w = 0.2$	$T_{flow} = 0.2$

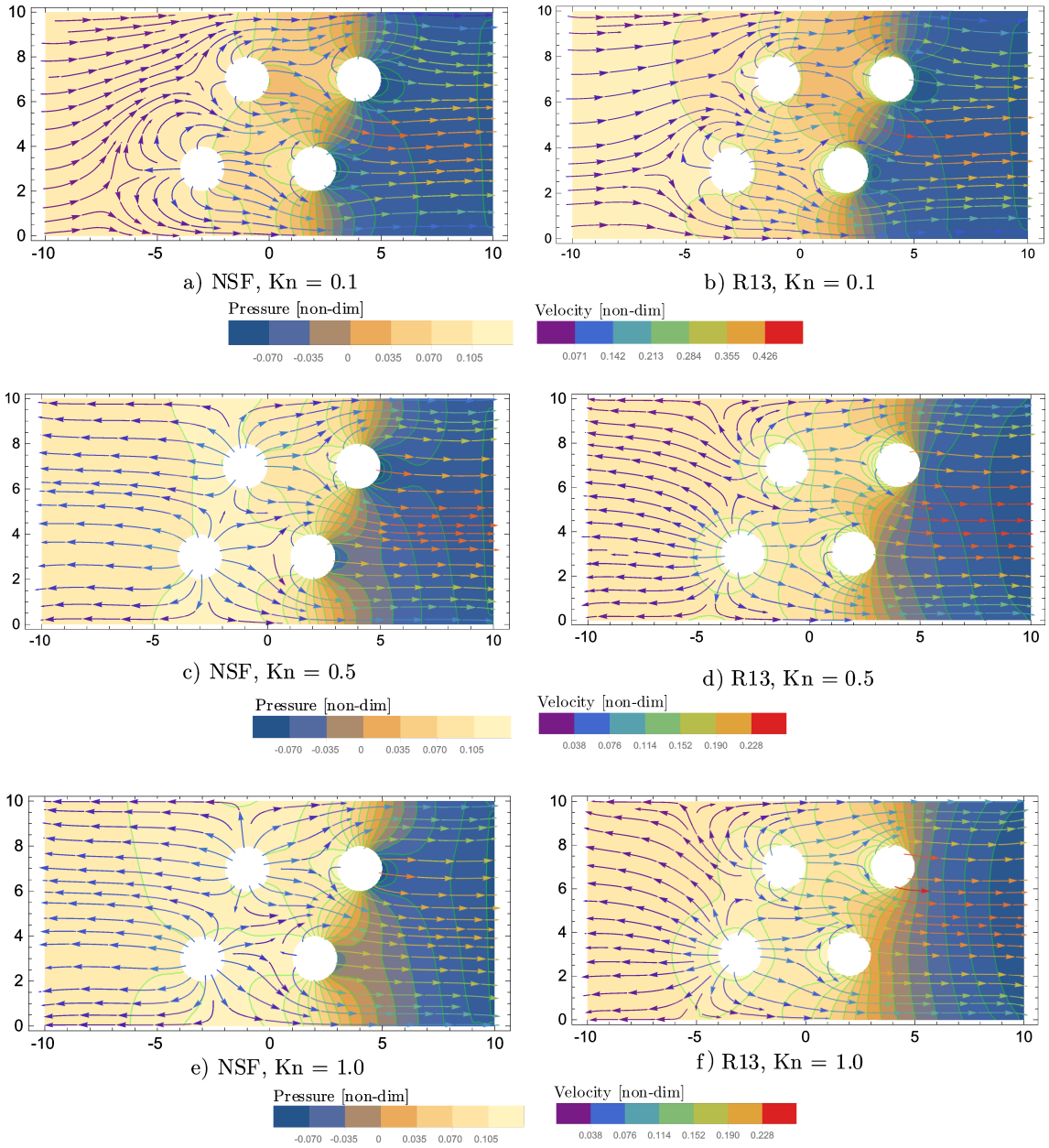

Figure 12. Pressure contours superimposed by velocity streamlines for two-dimensional channel-flow with four evaporating cylinders and various Knudsen numbers.

For Kn = 0.1, the velocity streamlines are similar between R13 and NSF. The inflow of the left boundary collides with the evaporating flow, which leaves the two cylinders on the left-hand side. The largest flow velocity is observed in between the two cylinders on the right-hand side. For Kn = 0.5, the evaporation overcomes the inflow and leaves the system at the inlet of the channel. This interesting effect is observed for R13 and NSF, but with different flow behavior. For R13, the streamlines, which leave the inlet, have their origin mainly in the left bottom cylinder. The dominance of the left cylinder

of R13 becomes even more apparent for Kn $= 1$. The NSF velocity streamlines at the inlet for Kn $= \{0.5, 1\}$ come almost equally from both cylinders on the left-hand side.

For Kn $= 0.1$, the pressure contours of R13 and NSF show very similar behavior. With increasing Kn, the R13-pressure contours on the right hand side of the diagrams disconnect from each other and become almost vertical for Kn $= 1$.

Also, for Kn $= 1$, significant differences between R13 and NSF are found for the temperature profiles, which are depicted in Fig. 13.

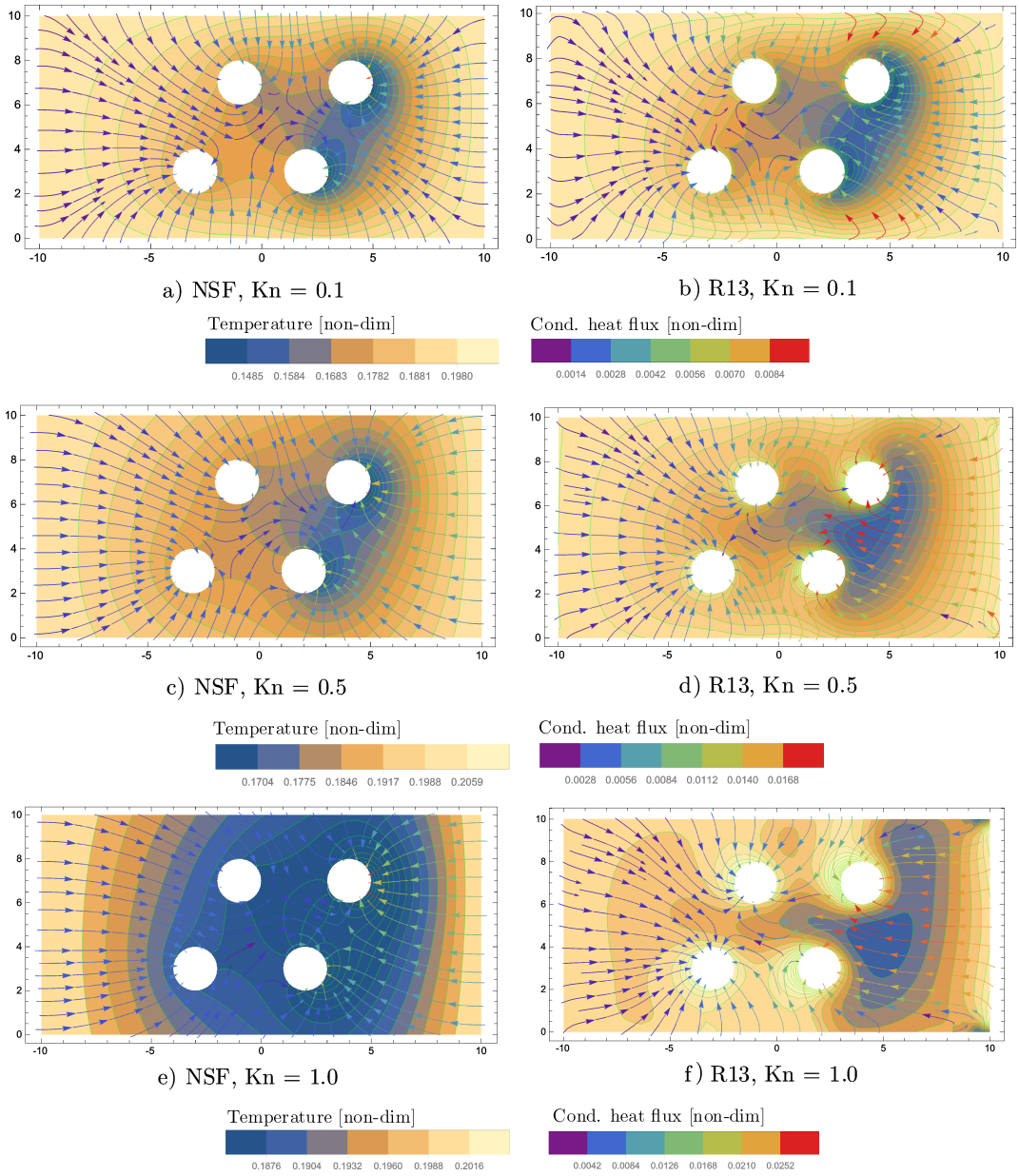

Figure 13. Temperature contours superimposed by cond. heat flux streamlines for two-dimensional channel-flow with four evaporating cylinders and various Knudsen numbers.

The overall temperature around the four evaporting cylinders is much lower for NSF, than for R13. As can be seen by the conductive heat flux streamlines, the enthalpy of vaporization is provided by the boundaries, as in the previous simulations. The magnitude of the R13 heat flux, shows interesting peaks in between the two cylinders on the right-hand side for Kn $= \{0.5, 1\}$.

The large differences between R13 and NSF for Kn $= \{0.5, 1\}$ are likely due to rarefaction effects, which can not be captured by NSF. It has to be taken into account, as mentioned in Sec. 4.2, that simplified NSF boundary conditions are used here. Note, that R13 is limited to flow regimes below Kn $= 1$ and can only describe a tendency here. For validation of the R13 results a reliable reference, such as from a DSMC simulation is necessary, which might be part of future work.

5. Conclusions

Based on the Onsager Theory, which utilizes the second law of thermodynamics, evaporation boundary conditions (PBC) for the R13 equations are derived. The Onsager coefficients have been determined by following a process consisting of three steps: In the first step (Sec. 3.1), the boundary conditions are compared with previously discussed boundary conditions for evaporation (MBC), which represent an alternative approach for deriving boundary conditions for R13. Under the assumption of proper results for MBC in the Navier-Stokes-Fourier (NSF) regime and by keeping in mind that higher moments develop a significant impact only for higher Knudsen numbers, coefficients are being taken over from MBC to PBC so that the differences between the sets of boundary conditions lie only in the terms with higher moments [12]. The idea is to find boundary conditions, which are just as reliable as MBC in the NSF regime and more accurate in the rarefied gas regime. In the next step, adjustable coefficients are suggested for the PBC. These coefficients are fitted by trial and error to DSMC data for the analytical solution of a finite, one-dimensional system (Sec. 3.3). In the third step for finding meaningful Onsager coefficients, the half space problem (Sec. 3.4) is solved analytically and ratios suggested by Ytrehus [15] are used to fine tune the coefficients. The overall agreement between PBC and DSMC (Sec. 3.5 and 3.6) has been shown to be better than for MBC/NSF and DSMC. Even though, there are differences in the higher order terms, when setting the adjustable coefficients $a = b... = f$ of the PBC to unity, the maximum deviation to the MBC, for the boundary values of the finite problem, is in the order of magnitude of $\pm 10^{-7}$, only.

For a general approach to convert MBC to PBC, with differences in the higher order terms only, see [17]. The impact of the evaporation and accommodation coefficients is discussed in Sec. 3.7. In Sec. 3.8 it is explained, how the trial and error fitting gives an insight into the meaning of the individual Onsager coefficients.

Due to lack of a mathematical approach for the fitting, i.e., an optimization algorithm, it is uncertain if significantly better fittings for the presented problems are possible. This may be part of a future analysis. Even though, NSF fails to predict normal stress for the presented systems, it shows surprisingly good results for low to moderate Knudsen Numbers. The advantage of R13 with PBC compared to NSF might be shown even more clearly in numerical simulations for complex geometries. The Onsager coefficients appear to be dependent on the evaporating material, which in the practical application becomes problematic. Therefore we recommend an investigation considering the fitting of Onsager coefficients as function of the enthalpy of vaporization, which defines the material.

In Sec. 4 the new evaporation/condensation boundary conditions are implemented into a code for the numerical solution of two-dimensional, steady-state problems. Results for Knudsen numbers of Kn={0.1,0.5,1.0} are obtained and compared to simplified Navier-Stokes-Fourier solutions. It is observed that with increasing Knudsen number, R13 shows different flow behavior than NSF.

It is necessary to compare these results to a reliable reference, such as a DSMC solution, which shall be a future effort. Additionally it might be of interest to compare the numerical R13 results to those of a 26-moment method, see [22].

Acknowledgments: We gratefully acknowledge the collaboration with Dr. Frezzotti, Politecnico de Milano, Italy, who provided the DSMC results. A.F.B. and H.S. are supported by the Natural Sciences and Engineering Research Council (NSERC). A.S.R. thankfully acknowledges the funding from EPSRC grant EP/N016602/1 in the UK and European Union's Horizon 2020 research and innovation program under the Marie Sklodowska Curie grant agreement no. 713548.

Author Contributions: This work is based on the M.A.Sc. thesis of A.F.B., who wrote the paper. A.F.B. was supervised by H.S. and advised by A.S.R. and M.T., who critically revised the paper. M.T. supervised A.F.B. during the process of implementing the new boundary conditions into the code of Torrilhon & Sarna, which provided the numerical results in Sec. 4.

Conflicts of Interest: The authors declare no conflict of interest.

Appendix Normal and tangential components

Within the process of deriving Onsager boundary conditions, it is desirable to decompose the tensors into their respective normal and tangential components. The normal component of a vector can be defined as

$$q_n = q_k n_k \,, \tag{A.1}$$

with its tangential component

$$\overline{q}_i = q_i - q_n n_i \,, \text{ with } \overline{q}_i n_i = 0 \,. \tag{A.2}$$

Similar one may define the components of a symmetric and trace-free tensor as [12]

$$\sigma_{nn} = \sigma_{rk} n_k n_r \,, \tag{A.3}$$

$$\overline{\sigma}_{ni} = \sigma_{ik} n_k - \sigma_{nn} n_i \,, \text{ with } \overline{\sigma}_{ni} n_i = 0 \,, \tag{A.4}$$

$$\widetilde{\sigma}_{ij} = \sigma_{ij} - \sigma_{nn}\left(\frac{3}{2} n_i n_j - \frac{1}{2}\delta_{ij}\right) - \overline{\sigma}_{ni} n_j - \widetilde{\sigma}_{nj} n_i \,, \text{ with } \widetilde{\sigma}_{ij} n_j = \widetilde{\sigma}_{kk} = 0 \,. \tag{A.5}$$

Here, σ_{nn} is the normal-normal component, $\overline{\sigma}_{ni}$ the normal-tangential component and $\widetilde{\sigma}_{ij}$ the tangential-tangential component. As mentioned in Sec. 1.2, the Einstein notation does not apply for index n. Similar for a symmetric and trace-free third order tensor, i.e., a 3-dimensional matrix one finds

$$m_{nnn} = m_{ijk} n_i n_j n_k \,, \tag{A.6}$$

$$\overline{m}_{nni} = m_{ijk} n_j n_k - m_{nnn} n_i \,, \text{ with } \overline{m}_{nni} n_i = 0 \,, \tag{A.7}$$

$$\widetilde{m}_{nij} = m_{ijk} n_k - m_{nnn}\left(\frac{3}{2} n_i n_j - \frac{1}{2}\delta_{ij}\right) - \overline{m}_{nni} n_j - \overline{m}_{nnj} n_i \,, \text{ with } \widetilde{m}_{nij} n_j = 0 \,. \tag{A.8}$$

Additionally one has:

$$\delta_{ij}\overline{m}_{nnj} n_i = \delta_{ij}\overline{\sigma}_{nj} n_i = \delta_{ij}\widetilde{m}_{nij} = 0 \,, \tag{A.9}$$

$$\delta_{ij} n_i n_j = n_j n_j = 1 \,. \tag{A.10}$$

Appendix Derivation of entropy fluxes

Based on the incompressible Navier-Stokes-Fourier-equations, a reduced entropy flux Ψ_k^l for the liquid side of a liquid-gas interface shall be derived in the following. Here, the vapor is a monatomic ideal gas with specific heat $c_p = \frac{5}{2}R$ and the liquid is described as an incompressible simple liquid. The heat of vaporization at reference state T_0, $p_{sat}(T_0)$ is

$$h_{gl}^0 = h^g(T_0) - h^l(T_0) = \frac{5}{2} R T_0 - \left(c_l T_0 + \frac{p_{sat}(T_0)}{\rho_l} + h_0\right) \,, \tag{B.1}$$

with the enthalpies

$$h^l = c_l (T - T_0) + \frac{5}{2} R T_0 + \frac{p - p_{sat}(T_0)}{\rho_l} - h_{gl}^0 \,, \tag{B.2}$$

$$h^g = \frac{5}{2} R T \,. \tag{B.3}$$

The energy density of the liquid $\varepsilon^l = \rho_l u^l$, with u^l as the internal energy, is

$$\varepsilon^l = \rho_l \left(h^l - \frac{p}{\rho_l} \right) = \rho_l \left(c_l \left(T - T_0 \right) + \frac{5}{2} R T_0 - \frac{p_{sat}\left(T_0\right)}{\rho_l} - h^0_{gl} \right) . \tag{B.4}$$

The entropy density $\eta^l = \rho_l s^l$ of the incompressible liquid is given as

$$\eta^l = c_l \rho_l \ln \frac{T^l}{T_0} - \frac{\rho_l}{T_0} h^0_{gl} , \tag{B.5}$$

where the proper entropy difference at equilibrium state $\frac{\eta^v(T_0)}{\rho^v} - \frac{\eta^l(T_0)}{\rho_l} = \frac{h^0_{gl}}{T_0}$ was used. The conservation laws for mass, energy and entropy for a fluid are

$$\frac{\partial \rho}{\partial t} + \frac{\partial \rho v_k}{\partial x_k} = 0 , \tag{B.6}$$

$$\frac{\partial \left(\varepsilon + \frac{\rho}{2} v^2 \right)}{\partial t} + \frac{\partial \left(\left(\varepsilon + \frac{\rho}{2} v^2 \right) v_k + q_k + p v_k + \sigma_{ik} v_i \right)}{\partial x_k} = 0 , \tag{B.7}$$

$$\frac{\partial \eta}{\partial t} + \frac{\partial \left(\eta v_k + \phi_k \right)}{\partial x_k} = \sigma_{gen} , \tag{B.8}$$

with $\eta v_k + \phi_k = \Psi_k$ as sum of convective and conductive entropy flux. When one intends linearized balance laws, the entropy must be considered up to quadratic terms in deviations from equilibrium. Motivated by entropy for the vapor given in Ref. [19], η is replaced by a linear combination α

$$\alpha = \eta + \frac{5}{2} R \rho - \frac{1}{T_0} \left(\varepsilon + \frac{\rho}{2} v^2 \right) , \tag{B.9}$$

which obeys the balance laws (B.6-B.8). Then, the reduced entropy balance reads

$$\frac{\partial \alpha}{\partial t} + \frac{\partial \left(\alpha v_k + \phi_k - \frac{1}{T_0} \left(p v_k + q_k + \sigma_{ik} v_i \right) \right)}{\partial x_k} = \Sigma_{gen} . \tag{B.10}$$

For deriving the entropy flux on liquid side, incompressible NSF is used with $\phi_k = \frac{q^l_k}{T^l}$ for the conductive part of the entropy flux. Hence the reduced entropy flux can be read from (B.10) as

$$\Omega^l_k = \alpha^l v^l_k + \frac{q^l_k}{T^l} - \frac{1}{T_0} \left(q^l_k + p^l v^l_k + \sigma^l_{ik} v^l_i \right) . \tag{B.11}$$

By using the equations of state for a liquid, (B.4, B.5) in (B.9) and after linearizing and non-dimensionalizing with (1), the reduced entropy density $\widetilde{\eta}^l$ obtains the form

$$\widetilde{\eta}^l = \frac{\alpha^l}{R \rho_l} = \frac{p_{sat}\left(T_0\right)}{\rho_l R T_0} - \frac{c_l}{R} \frac{\left(\widehat{T}^l \right)^2}{2} - \frac{1}{2} \left(\widehat{v}^l \right)^2 . \tag{B.12}$$

The reduced entropy flux (dimensionless, linearized) on liquid side which, depending on evaporation or condensation, either enters or leaves the interface between liquid and vapor follows as

$$\Psi^l_k = \frac{\Omega^l_k}{\rho_0 R \sqrt{R T_0}} = -\widehat{p}^l \widehat{v}^l_k - \widehat{q}^l_k \widehat{T}^l - \widehat{\sigma}^l_{ik} \widehat{v}^l_i . \tag{B.13}$$

The hats, which denote dimensionless deviations from the respective equilibrium state are neglected in Sec. 3. By considering R13 for the vapor phase, the entropy for vapor can be found in the same manner,

over a linear combination of (B.6-B.8). Though due to the higher moments, there are additional terms in the (dimensionless, linearized) reduced entropy density $\widetilde{\eta}^g$ and reduced entropy flux Ψ_k^g, see Ref. [19]:

$$\widetilde{\eta}^g = \widehat{\eta}_0 - \frac{\left(\widehat{\rho}^g\right)^2}{2} - \frac{\left(\widehat{v}^g\right)^2}{2} - \frac{3}{4}\left(\widehat{T}^g\right)^2 - \frac{\omega_2}{8}\left(\widehat{\sigma}^g\right)^2 - \frac{2\theta_2}{25}\left(\mathrm{Pr}\right)^2\left(\widehat{q}^g\right)^2 , \tag{B.14}$$

$$\Psi_k^g = -\widehat{p}^g\widehat{v}_k^g - \widehat{q}_k^g\widehat{T}^g - \widehat{\sigma}_{ik}^g\widehat{v}_i^g - \frac{\omega_3}{5}\,\mathrm{Pr}\,\widehat{q}_i^g\widehat{\sigma}_{ik}^g - \frac{\omega_2}{4}\widehat{\sigma}_{ij}^g\widehat{m}_{ijk} - \frac{2\theta_2}{25}\left(\mathrm{Pr}\right)^2\left(\widehat{q}_i^g\widehat{R}_{ik} + \frac{\widehat{\Delta}}{3}\widehat{q}_k^g\right) . \tag{B.15}$$

Appendix Comparison PBC vs. MBC for non-fitted coefficients

For Maxwell molecules, the normal boundary conditions of PBC and MBC are compared with each other. The Onsager coefficients (31-36) are plugged into the PBC, which consist of normal components (28), while considering data for Maxwell molecules from Table 1 and setting the adjustable coefficients $a = b = ... = f = 1$:

$$V_n^g = \sqrt{\frac{2}{\pi}}\frac{\vartheta}{2-\vartheta}\left(p_{sat}\left(T^l\right) - p^g - \frac{1}{2}\sigma_{nn}^g + \frac{1}{2}\left(T^g - T^l\right) + \underline{\frac{1}{30}\Delta} + \underline{\frac{1}{10}R_{nn}}\right) , \tag{C.1}$$

$$q_n^g = -\sqrt{\frac{2}{\pi}}\frac{\vartheta + \chi(1-\vartheta)}{2-\vartheta-\chi(1-\vartheta)}\left(2\left(T^g - T^l\right) + \frac{1}{2}\sigma_{nn}^g + \underline{\frac{2}{15}\Delta} + \underline{\frac{2}{5}R_{nn}}\right) - \frac{1}{2}V_n^g , \tag{C.2}$$

$$m_{nnn} = \sqrt{\frac{2}{\pi}}\frac{\vartheta + \chi(1-\vartheta)}{2-\vartheta-\chi(1-\vartheta)}\left(\frac{2}{5}\left(T^g - T^l\right) - \frac{7}{5}\,\sigma_{nn}^g + \underline{\frac{2}{75}\Delta} + \underline{\frac{2}{25}R_{nn}}\right) - \frac{2}{5}V_n^g . \tag{C.3}$$

The terms, that are different between PBC and MBC are underlined. All lower order terms, i.e., p^g, σ_{nn} and $\left(T^g - T^l\right)$ are equal between PBC and MBC, whereas the higher order terms Δ and R_{nn} differ, see Sec. 1.2.

Appendix Onsager Boundary Conditions for Navier-Stokes-Fourier

Here, the Navier-Stokes-Fourier equations are used together with evaporation boundary conditions, based on the Onsager theory. For full evaporation $\vartheta = 1$, fully diffusive reflection $\chi = 1$ and by considering one-dimensional heat and mass transfer only, the boundary conditions are given as [23][11]

$$\begin{bmatrix} \frac{p_{sat}-p^g}{\sqrt{2\pi}} \\ \frac{\left(T^l-T^g\right)}{\sqrt{2\pi}} \end{bmatrix} = \begin{bmatrix} r_{11} & r_{12} \\ r_{21} & r_{22} \end{bmatrix} \begin{bmatrix} v_x^g \\ q_x^g \end{bmatrix} . \tag{D.1}$$

All variables are non-dimensional and linearized. The matrix of Onsager coefficients read [23][11]

$$r_{\alpha\beta} = \begin{bmatrix} \left(\frac{1}{\vartheta} - \frac{1}{2}\right) + \frac{1}{16} & \frac{1}{8} \\ \frac{1}{8} & \frac{1}{4} \end{bmatrix} . \tag{D.2}$$

The solutions based on D.2 are referred to as uncorrected NSF. A correction can be found in kinetic theory, which yields [23][11]

$$r_{\alpha\beta,corr} = \begin{bmatrix} \frac{1}{\vartheta} - 0.40044 & 0.126 \\ 0.126 & 0.291 \end{bmatrix} . \tag{D.3}$$

References

1. Cercignani, C. *Theory and application of the Boltzmann equation*; Scottish Academic Press, Edinburgh, Scottland, 1975.
2. Kremer, G. *An Introduction to the Boltzmann Equation and Transport Processes in Gases*; Springer, Berlin/Heidelberg, Germany, 2010.
3. Bird, G.A. *Molecular gas dynamics and the direct simulation of gas flows*; Oxford University Press, Oxford, United Kingdom, 1994.
4. Torrilhon, M. Modeling Nonequilibrium Gas Flow Based on Moment Equations. *Annu. Rev. Fluid Mech.* **2008**, *48*, 429-458.
5. Struchtrup, H. *Macroscopic Transport Equations for Rarefied Gas Flows - Approximation Methods in Kinetic Theory*; Interaction of Mechanics and Mathematics Series, Springer, Heidelberg, Germany, 2005.
6. Struchtrup, H.; Torrilhon, M. Higher-order effects in rarefied channel flows. *Phys. Rev.* **2008**, *78*, 046301.
7. Rana, A.; Mohammadzadeh, A.; Struchtrup, H. A numerical study of the heat transfer through a rarefied gas confined in a micro cavity. *Continuum Mech. Thermodyn.* **2015**, *27*, 433-446.
8. Mohammadzadeh, A.; Struchtrup, H. Velocity dependent Maxwell boundary conditions in DSMC," Int. Journal of Heat and Mass Transfer. *Int. Journal of Heat and Mass Transfer* **2015**, *87*, 151-160.
9. Struchtrup, H.; Torrilhon, M. Regularization of Grad's 13 moment equations: Derivation and linear analysis. *Phys. Fluids* **2003**, *15*, 2668-2680.
10. Karniadakis, G.; Beskok, A.; Aluru, N. *Microflows and Nanoflows: Fundamentals and simulation*; Springer, New York, USA, 2005.
11. Struchtrup H.; Beckmann, A.; Rana, A.S.; Frezzotti, A. Evaporation boundary conditions for the R13 equations of rarefied gas dynamics *Phys. Fluids* **2017**, *29*, 092004.
12. Rana, A.S.; Struchtrup, H. Thermodynamically admissible boundary conditions for the regularized 13 moment equations. *Phys. Fluids* **2016**, *28*, 027105.
13. Kjelstrup, S.; Bedeaux, D.; Johannessen, E.; Gross, J. *Non-Equilibrium Thermodynamics for Engineers*; World Scientific, Singapore, 2010.
14. Kjelstrup, S.; Bedeaux, D. *Non-Equilibrium Thermodynamics of Heterogeneous Systems*; World Scientific, Singapore, 2008.
15. Ytrehus, T. *Kinetic Theory Description and Experimental Results for Vapor Motion in Arbitrary Strong Evaporation*; Technical Note 112, Von Karman Institute for Fluid Dynamics, 1975.
16. Bond, M.; Struchtrup, H. Mean evaporation and condensation coefficients based on energy dependent condensation probability *Phys. Rev.* **2004**, *70*, 061605.
17. Sarna, N.; Torrilhon, M. On Stable Wall Boundary Conditions for the Hermite Discretization of the Linearised Boltzmann Equation. *J. Stat. Phys.* **2018**, *170*, 101-126.
18. Struchtrup, H. *Thermodynamics and Energy Conversion*; Springer, Heidelberg, Germany, 2014.
19. Struchtrup, H.; Torrilhon, M. H theorem, Regularization, and Boundary Conditions for Linearized 13 Moment Equations. *Phys. Rev. Lett.* **2007**, *99*, 014502.
20. de Groot, S.R.; Mazur, P. *Non-Equilibrium Thermodynamics*; North-Holland Publishing Company, Amsterdam, Netherlands, 1962.
21. Torrilhon, M.; Sarna, N. Hierarchical Boltzmann simulations and model error estimation. *Journal of Computational Physics* **2017**, *342*, 66-84.
22. Rana, A.S.; Lockerby, D.; Sprittles, J. Evaporation-driven vapour microflows: analytical solutions from moment methods. *Journal of Fluid Mechanics* **2018**, *841*, 962-988.
23. Caputa, J.P.; Struchtrup, H. Interface model for non-equilibrium evaporation. *Physica A* **2011**, *390*, 31-42.